



This is a repository copy of *SPH based numerical treatment of the interfacial interaction of flow with porous media*.

White Rose Research Online URL for this paper:
<https://eprints.whiterose.ac.uk/152675/>

Version: Accepted Version

Article:

Kazemi, E. orcid.org/0000-0002-1780-1846, Tait, S. and Shao, S. (2020) SPH based numerical treatment of the interfacial interaction of flow with porous media. *International Journal for Numerical Methods in Fluids*, 92 (4). pp. 219-245. ISSN 0271-2091

<https://doi.org/10.1002/fld.4781>

This is the peer reviewed version of the following article: Kazemi, E, Tait, S, Shao, S. SPH Based Numerical Treatment of the Interfacial Interaction of Flow with Porous Media. *Int J Numer Meth Fluids*. 2019., which has been published in final form at <https://doi.org/10.1002/fld.4781>. This article may be used for non-commercial purposes in accordance with Wiley Terms and Conditions for Use of Self-Archived Versions.

Reuse

Items deposited in White Rose Research Online are protected by copyright, with all rights reserved unless indicated otherwise. They may be downloaded and/or printed for private study, or other acts as permitted by national copyright laws. The publisher or other rights holders may allow further reproduction and re-use of the full text version. This is indicated by the licence information on the White Rose Research Online record for the item.

Takedown

If you consider content in White Rose Research Online to be in breach of UK law, please notify us by emailing eprints@whiterose.ac.uk including the URL of the record and the reason for the withdrawal request.



eprints@whiterose.ac.uk
<https://eprints.whiterose.ac.uk/>

SPH Based Numerical Treatment of the Interfacial Interaction of Flow with Porous Media

Ehsan Kazemi, Simon Tait, Songdong Shao

Department of Civil & Structural Engineering, University of Sheffield, Sheffield S1 3JD, UK

Abstract

In this paper, the macroscopic equations of mass and momentum are developed and discretised based on the Smoothed Particle Hydrodynamics (SPH) formulation for the interaction at an interface of flow with porous media. The theoretical background of flow through porous media is investigated in order to highlight the key constraints which should be satisfied, particularly at the interface between the porous media flow and the overlying free flow. The study aims to investigate the derivation of the porous flow equations, computation of the porosity, and treatment of the interfacial boundary layer. It addresses weak assumptions that are commonly adopted for interfacial flow simulation in particle-based methods. As support to the theoretical analysis, a 2D weakly compressible SPH (WCSPH) model is developed based on the proposed interfacial treatment. The equations in this model are written in terms of the intrinsic averages and in the Lagrangian form. The effect of particle volume change due to the spatial change of porosity is taken into account and the extra stress terms in the momentum equation are approximated by using Ergun's equation and the Sub-Particle Scale (SPS) model to represent the drag and turbulence effects, respectively. Four benchmark test cases covering a range of flow scenarios are simulated to examine the influence of the porous boundary on the internal, interface and external flow. The capacity of the modified SPH model to predict velocity distributions and water surface behaviour is fully examined with a focus on the flow conditions at the interfacial boundary between the overlying free flow and the underlying porous media.

Keywords: SPH, porous media, interfacial flow, fluid-solid interaction, intrinsic average, free surface flow.

1 Introduction

When water waves interact with a porous body, a part of the wave energy dissipates due to the permeability of the porous body. Hence, structures with significant porosity are widely used in coastal areas to mitigate the effects of wave attack on structures and beaches. Understanding the mechanisms of the flow, especially the momentum transfer between the flow and porous structure is of great importance for the engineers in order to improve the design of coastal protection structures.

Currently, numerical simulations have been extensively used for the investigation of the interaction between water waves and flows within porous bodies. The most desirable approach would be to solve the governing equations at the microscopic (pore) level, where all geometrical characteristics of the porous media as well as all scales of the flow are resolved through a Direct Numerical Simulation. However, this is often impractical due to the limitations in practical computational power. Therefore, the macroscopic approach is used more widely by modellers in engineering contexts, in which the porous medium is represented as a single-phase continuum and the frictional effects of the solid matrix on the macroscopic field are incorporated as extra drag terms in the governing equations. Many earlier numerical models for porous flow simulation have been developed on grid-based approaches, such as the Finite Difference or Finite Volume Methods, where a fixed grid system is used in the Eulerian framework. Recently, particle-based modelling approaches, such as the SPH and Moving Particle Semi-implicit (MPS), have been received extensive interest due to their capacity in efficiently simulating complex fluid motions, particularly those with large free surface deformation and discontinuous boundaries, through a Lagrangian framework (for the latest advancement in this field, see Gotoh and Khayyer, 2018). In spite of its wide application in coastal hydrodynamics, only a small number of SPH studies have focussed on the simulation of flow interaction with porous structures mainly due to the difficulties in developing robust treatments of the interfacial boundary flow.

One of the first SPH applications for the interaction of flow with porous media was delivered by Shao (2010), who used an incompressible SPH (ISPH) model constructed from the macroscopic equations of Huang et al. (2003). In their treatment of interfacial boundary, the computational domain was separated into porous and free-flow (clear water) sub regions and the matching conditions of velocity and normal and tangential stresses were imposed at the interface between these defined sub regions. However, the effects of flow turbulence and volume change of fluid particles inside the solid skeleton of the physical porous zone were not considered. In a later improvement, Akbari and Namin (2013) used the local Volume-Averaged Navier-Stokes (N-S) equations and solved a unified set of governing equations within a single computational domain by introducing a transitional layer at the interface between overlying free-flow region and porous media. A background mesh was used, where the porosity at the position of SPH particles was calculated by averaging the reference porosity of neighbouring mesh points over an interpolating area using the SPH interpolation method with a smoothing length h_γ of the scale of the mean grain diameter in the porous media. They set the thickness of the interfacial transitional layer (over which the fluid-solid porosity is variable) to be 4 times the particle diameter in the porous media. Gui et al. (2015) adopted the transitional layer approach of Akbari and Namin (2013) aiming to improve the early porous flow model of Shao (2010). However, this model still ignored the effects of flow turbulence and porosity variation in the governing equations. Akbari (2014) improved the previous model of Akbari and Namin (2013) by explicitly incorporating a standard SPS turbulence closure into their ISPH model for the wave interaction with multi-layered porous structures. In both Akbari and Namin (2013) and Akbari (2014), good agreement was found in the water surface profiles in the free-flow zone, but no comparison was made with the velocity distribution especially within the interfacial boundary layer.

Ren et al. (2014) employed the spatially averaged N-S equations, in which a transitional layer was used at the interfacial boundary to separate the free-flow region and the flow in the underlying porous media. Then, the velocity of a certain particle in the interfacial layer was calculated by using only its neighbouring particles of the same type; and finally interpolated using all its neighbouring particles of both types. The SPS turbulent model with the Smagorinsky coefficient of $C_s = 0.1$ was applied only in the free-flow region, while the

effect of turbulence in the porous media region was ignored. The thickness of the transitional layer was set to the size of one smoothing length, which means it was related only to the computational resolution rather than the physical length scales of the flow or porous media at the interface. In a follow-on study, Ren et al. (2016) improved their previous work by using the Volume-Averaged and Favre-Averaged N-S equations along with the SPS turbulence closure model for the flows both inside and outside the porous media. Regarding the interfacial boundary treatment, they applied a transitional interface layer that is similar to the treatment of Akbari and Namin (2013) but with the thickness of the layer being set to one mean diameter of the solid particles of porous medium. Pahar and Dhar (2016; 2017) developed ISPH models to simulate the interaction of flows with porous media. The interfacial boundary conditions were implicitly implemented by representing the Darcy velocity in the governing equations and incorporating the porosity parameter into the Pressure Poisson Equation (PPE). The effective viscosity in free-flow region was calculated as the summation of the SPS eddy viscosity and the actual fluid viscosity; while inside the porous media the effective viscosity was set equal to actual viscosity of the fluid only. To alleviate the discontinuity of viscosity at the interfacial boundary, the fluid part of the viscosity of free-flow region and the viscosity of the fluid in the porous media were averaged (Pahar and Dhar, 2016). Moreover, due to the change of porosity, they arbitrarily adopted a concept of a non-constant smoothing length in the formulation (Pahar and Dhar, 2017). Recently, Khayyer et al. (2018) developed an enhanced ISPH model based on two-phase mixture theory to simulate the interaction of waves with porous media of variable porosity. They incorporated the effect of porosity using linear and nonlinear resistance force terms in the N-S equations as well as a newly derived source term in the PPE. The results showed smooth and continuous pressure fields at the interfacial boundary without applying any artificial smoothing schemes.

In summary, SPH has shown a capacity in macroscopically simulating the flow interactions with porous media. However, as discussed above, it still has some limitations such as that i) in most model validations, the water surface elevations were often compared with the experimental data, while the velocity field, particularly around the surface of porous structures, was not investigated in detail; and more importantly, ii) the interface boundary

layer between the porous and free-flow regions was usually treated based on numerical calibrations rather than with rigorous mathematical and physical justifications, and little effort was made to investigate the behaviour of flow in this interfacial boundary layer. Being motivated by these limitations, in this paper, we firstly develop the SPH macroscopic governing equations for the flow interactions with porous media to clearly show the key limitations and constraints with the current particle-based averaging approaches, and further provide physically sound and practical computational solutions to address these limitations. Then, a 2D WCSPH model is developed and applied to four benchmark cases of free-flow interaction with porous media. Validation is carried out through the comparisons of both water surface profiles and velocity distributions with a focus on the behaviour of the flows within and close to the interfacial boundary.

2 Theoretical Background and Model Development

A system containing two phases α and β , which represent the fluid and solid phases respectively, is considered. The full form of the compressible version of microscopic conservation equations of mass and momentum (Eqs. 1 and 2) is used as the governing equations at the pore level:

$$\gamma \frac{\partial \rho}{\partial t} + \gamma \nabla \cdot (\rho \mathbf{u}) = 0 \quad (1)$$

$$\gamma \frac{\partial (\rho \mathbf{u})}{\partial t} + \gamma \nabla \cdot (\rho \mathbf{u} \mathbf{u}) = -\gamma \nabla P + \gamma \rho \mathbf{g} + \gamma \mu \nabla^2 \mathbf{u} \quad (2)$$

where t is the time; ρ , \mathbf{u} and P are the density, velocity and pressure, respectively, at the pore level; \mathbf{g} is the gravitational acceleration; μ is the dynamic fluid viscosity; and γ is a distribution function associated with the α -phase. Following Grey and Lee (1977), the distribution function is set to one for the α -phase (fluid), and zero for the β -phase (solid) as given in Eq. (3). This means any property like ψ and its temporal and spatial derivatives are respectively, ψ , $\partial\psi/\partial t$ and $\nabla\psi$ in the α (fluid)-phase, and zero in the β (solid)-phase.

$$\gamma = \begin{cases} 1, & \alpha\text{-phase} \\ 0, & \beta\text{-phase} \end{cases} \quad (3)$$

2.1 Macroscopic governing equations

The microscopic equations (Eqs. 1 and 2) are spatially averaged over an averaging volume Ω , which is representative of the whole system at time t , using a weighting function G which satisfies the three principles presented in Quintard and Whitaker (1994) as well as the symmetry condition. Assuming the solid phase (β) is fixed in time and space, adopting a method similar to that used by Quintard and Whitaker (1994) to derive the macroscopic Stokes equations, adding the effect of turbulence in the form of Large Eddy Simulation (LES), transferring the Eulerian form of the equations to the Lagrangian one, and expressing the averaged equations in terms of the intrinsic averages, the macroscopic governing equations of mass and momentum can be written as follows (see Appendix A for details, and Kazemi (2017) for the full derivation process),

$$(G * \gamma) \frac{D\langle\rho\rangle^\alpha}{Dt} + \langle\rho\rangle^\alpha \nabla \cdot [(G * \gamma)\langle\mathbf{u}\rangle^\alpha] = 0 \quad (4)$$

$$(G * \gamma)\langle\rho\rangle^\alpha \frac{D\langle\mathbf{u}\rangle^\alpha}{Dt} = -(G * \gamma)\nabla\langle P\rangle^\alpha + (G * \gamma)\langle\rho\rangle^\alpha \mathbf{g} + \mu\nabla^2[(G * \gamma)\langle\mathbf{u}\rangle^\alpha] \\ - \mu\nabla\langle\mathbf{u}\rangle^\alpha \nabla(G * \gamma) - \nabla \cdot [(G * \gamma)\langle\boldsymbol{\tau}\rangle^\alpha] + G * [(-\mathbf{I}\tilde{P}^\alpha + \mu\nabla\tilde{\mathbf{u}}^\alpha)\mathbf{n}_{\alpha\beta}\delta_{\alpha\beta}] \quad (5)$$

where $G * ()$ denotes the convolution product of the weighting function G and the corresponding variable; and $\langle \rangle^\alpha$ denotes the α -phase (fluid) intrinsic average operator. In the last term on the right-hand side of Eq. (5), \tilde{P}^α and $\tilde{\mathbf{u}}^\alpha$ denote the spatial deviations of the point pressure and velocity from their intrinsic average; \mathbf{I} is the unit tensor; $\mathbf{n}_{\alpha\beta}$ is the unit normal vector pointing from the α -phase to the β -phase; and $\delta_{\alpha\beta}$ is the Dirac distribution associated with the $\alpha - \beta$ interfaces. This surface integral term represents the frictional effect of the solid skeleton on the macroscopic field, and the second to last term on the right-hand side of Eq. (5) represents the effect of flow turbulence on the average flow field, where $\langle\boldsymbol{\tau}\rangle^\alpha$ is the SPS fluid stress tensor.

It should be noted that the following assumptions and constraints were imposed to obtain the present form of the equations (see Kazemi, 2017).

Constraint #1: $r_\Omega \gg L_\psi$ (6)

Constraint #2:
$$r_{\Omega} \ll L_{\langle\psi\rangle^{\alpha}} \quad (7)$$

where L_{ψ} is a microscopic characteristic length (pore scale) over which significant variations in the quantity ψ take place; $L_{\langle\psi\rangle^{\alpha}}$ is the characteristic length scale over which significant variations in the average of the quantity ψ take place; and r_{Ω} is the support of the weighting function G . It is noted that the constraint described in Eq. (7) is defined in terms of the intrinsic average $\langle\psi\rangle^{\alpha}$. Whitaker (1969) defined these two constraints ‘intuitively’ to ensure that the averaging volume is ‘large enough’ to contain all the essential geometrical characteristics of the porous medium; and ‘small enough’ so that the size of the averaging volume is negligible compared with the macroscopic region.

Constraint #3: the averaging volume Ω (and the weighting function G) should not change with local time. In other words, they should remain unchanged relative to the centroid of the volume over the total (material) time.

Assumption #1: for fluid quantities, the superficial volumetric average of spatial deviations from the intrinsic average, i.e. $\tilde{\psi}^{\alpha}$, at the centroid of the averaging volume is negligible: $G * (\gamma\tilde{\psi}^{\alpha}) \approx 0$.

Assumption #2: no-slip boundary conditions are applied at the solid-fluid ($\alpha - \beta$) boundaries, i.e. $\mathbf{u}_{\alpha\beta} \cdot \mathbf{n}_{\alpha\beta} = 0$.

Assumption #3: the characteristic length scales of the density and its intrinsic average, L_{ρ} and $L_{\langle\rho\rangle^{\alpha}}$, respectively, are infinite values, i.e. the flow is incompressible. This assumption leads to the density being considered as a spatially constant value over the averaging volume, thus the developed equations are for incompressible fluid flow. However, the density is not truly constant in the present simulations (carried out in Section 3) due to the application of the WCSPH scheme. But, since the variations of density (compressibility of flow) will be restricted to be less than 1 % (see Sections 2.3 and 3.1), the effects of variability of density on the velocity field, LES, etc. is expected to be small.

From now on, Eqs. (4) and (5) need to be averaged based on the SPH formulations to transform the spatial derivatives of intrinsic averages into the SPH approximated ones,

which can be eventually translated into the SPH discretised forms by using summations over the discrete particles.

2.2 The SPHAM equations

The macroscopic equations of mass and momentum are now approximated based on a SPH scheme. A convolution product is applied to these equations but using a different weighting function from that used in deriving the macroscopic equations. Although the same function G could be used, a different notation is used for the weighting (kernel) function in order to distinguish the solution process on the macroscopic field from the determination of $G * \gamma$ on the microscopic field. Averaging the macroscopic equations (Eqs. 4 and 5) over an averaging volume Υ using a kernel function W , they are represented in the following SPH forms (for details see Kazemi, 2017) which will be later shown in their discretised form in Section 2.3.

$$\frac{D\langle\rho\rangle^\alpha}{Dt} = -\frac{\langle\rho\rangle^\alpha}{(G * \gamma)} \{\nabla W * [(G * \gamma)\langle\mathbf{u}\rangle^\alpha]\} \quad (8)$$

$$\begin{aligned} \frac{D\langle\mathbf{u}\rangle^\alpha}{Dt} = & -\frac{1}{\langle\rho\rangle^\alpha} (\nabla W * \langle P\rangle^\alpha) + \mathbf{g} + \frac{\mu}{(G * \gamma)\langle\rho\rangle^\alpha} \{\nabla W * \nabla[(G * \gamma)\langle\mathbf{u}\rangle^\alpha]\} \\ & - \frac{\mu\nabla(G * \gamma)}{(G * \gamma)\langle\rho\rangle^\alpha} (\nabla W * \langle\mathbf{u}\rangle^\alpha) - \frac{1}{(G * \gamma)\langle\rho\rangle^\alpha} \{\nabla W * [(G * \gamma)\langle\boldsymbol{\tau}\rangle^\alpha]\} \\ & + \frac{1}{(G * \gamma)\langle\rho\rangle^\alpha} \{G * [(-\mathbf{I}\tilde{P}^\alpha + \mu\nabla\tilde{\mathbf{u}}^\alpha)\mathbf{n}_{\alpha\beta}\delta_{\alpha\beta}]\} \end{aligned} \quad (9)$$

It should be noted that, the kernel function W should satisfy the Delta function property condition in addition to the conditions that the weighting function G needs to satisfy (see Section 2.1). Constraints similar to *constraints #2* and *#3* are also required for approximating the macroscopic field using the kernel function W over the averaging volume Υ (see Kazemi, 2017, for details). These constraints are that the support of the kernel function W (i.e. r_Υ) should be much smaller than the characteristic length scale of the average flow field, i.e. $r_\Upsilon \ll L_{(\psi)^\alpha}$ (*constraint #4*); and the averaging volume Υ (and the weighting function W) should not change with the local time, i.e. they should remain unchanged relative to the centroid of the volume over the total time (*constraint #5*). A constraint similar to *constraint #1* is not required to be imposed on the size of the support of the kernel function r_Υ , since in

the macroscopic description of the porous media, the domain is considered as a single-phase continuum.

Equations (8) and (9) are called the SPH-Averaged Macroscopic (SPHAM) equations of mass and momentum, respectively; and $G * \gamma$ is called the porosity and replaced with ϕ in the equations. These equations are defined in a unified framework, i.e. they describe the fluid motion over the entire computational domain including both the porous and free-flow regions. The usefulness of using distinct averaging operators (G and W) in the averaging process over the microscopic and macroscopic fields is evident in the above equations. As can be seen, the convolution products with W (which is the SPH averaging operator over the macroscopic field) contain intrinsic averages of fluid properties like $\langle \mathbf{u} \rangle^\alpha$ and $\langle P \rangle^\alpha$ which are problem unknowns. On the other hand, the convolution product of $G * \gamma$ contains the distribution function γ only, which is a property of the microscopic field that is a known variable over a fixed domain. Therefore, the practice of using a background mesh for the porosity computation (Akbari and Namin, 2013) is properly justified. As long as a background mesh is applied for this purpose, and the weighting function G is employed to calculate only porosity on an Eulerian fixed mesh, Ω and G of a moving element (particle) may change over the total time, but in a way that they do not change on the Eulerian domain. Therefore, *constraint #3* can be expressed as ‘ r_Ω and G should not change with time over the Eulerian domain’.

Equations (8) and (9) are similar to the equations used in other SPH studies (e.g. in Akbari and Namin, 2013; Ren et al., 2016; and Pahar and Dhar, 2016) with the difference that the present equations are developed and presented in terms of the intrinsic averages rather than the superficial ones. By solving the flow passing a moving porous cylinder, Wang et al. (2015) showed that the macroscopic equations defined in terms of the superficial average velocities could break the Galilean invariance while the equations with intrinsic averages do not have such a limitation. It is notable that the present mass equation (Eq. 8) is different from the one used in the ISPH studies in which the temporal derivative of the density is zero due to the incompressibility of flow. It also should be noted that this equation is slightly different from the continuity equation employed in Ren et al.’ (2016) WCSPH model. Rewriting the continuity equation in Ren et al. (2016) in terms of intrinsic averages of fluid

quantities to be comparable to the present mass equation, the porosity would disappear; while the presence of porosity $G * \gamma$ both inside the divergence term as well as in the denominator of the right-hand side of Eq. (8) leads to the capture of the variations of porosity over the interfacial boundary.

2.3 Discretisation of the equations and the domain

It is possible to discretise the SPHAM equations (Eqs. 8 and 9) so that they can be solved at the position of a set of discrete moving particles. The discretised version of these equations is written in the following symmetric form (for details see Kazemi, 2017).

$$\frac{\rho_a|^{(t+\Delta t)} - \rho_b|^{(t)}}{Dt} = \sum_b \frac{m_b}{\phi_a \phi_b} (\phi \mathbf{u})_{ab} \nabla_a W_{ab} \quad (10)$$

$$\begin{aligned} \frac{\mathbf{u}_a|^{(t+\Delta t)} - \mathbf{u}_b|^{(t)}}{\Delta t} = & - \sum_b \left\{ \frac{m_b}{\phi_b} \nabla_a W_{ab} \frac{P_a + P_b}{\rho_a \rho_b} \right\} + \mathbf{g} \\ & + \sum_b \left\{ \frac{\mu m_b}{\phi_a \phi_b} \frac{\mathbf{r}_{ab} \cdot \nabla_a W_{ab} 2(\phi \mathbf{u})_{ab} + \phi_{ab} \mathbf{u}_{ab}}{|\mathbf{r}_{ab}|^2 + \eta^2} \right\} \\ & - \sum_b \left\{ \frac{m_b}{\phi_a \phi_b} \nabla_a W_{ab} \cdot \frac{\phi_a \boldsymbol{\tau}_a + \phi_b \boldsymbol{\tau}_b}{\rho_a \rho_b} \right\} - \mathbf{A}_a \end{aligned} \quad (11)$$

where a and b denote the central particle and its neighbouring particles, respectively, in the averaging volume Υ ; m is the particle mass; $\rho_a = \langle \rho \rangle_a^\alpha$; $\rho_b = \langle \rho \rangle_b^\alpha$; $P_a = \langle P \rangle_a^\alpha$; $P_b = \langle P \rangle_b^\alpha$; $\mathbf{u}_a = \langle \mathbf{u} \rangle_a^\alpha$; $\mathbf{u}_b = \langle \mathbf{u} \rangle_b^\alpha$; $\boldsymbol{\tau}_a = \langle \boldsymbol{\tau} \rangle_a^\alpha$; $\boldsymbol{\tau}_b = \langle \boldsymbol{\tau} \rangle_b^\alpha$; $\mathbf{u}_{ab} = \langle \mathbf{u} \rangle_a^\alpha - \langle \mathbf{u} \rangle_b^\alpha$; $\phi_{ab} = \phi_a - \phi_b$; $(\phi \mathbf{u})_{ab} = \phi_a \langle \mathbf{u} \rangle_a^\alpha - \phi_b \langle \mathbf{u} \rangle_b^\alpha$; $\mathbf{r}_{ab} = \mathbf{r}_a - \mathbf{r}_b$; $\nabla_a W_{ab} = \nabla W(\mathbf{r}_a - \mathbf{r}_b, h_\Upsilon)$; $\eta = 0.1h_\Upsilon$; and \mathbf{A}_a is the approximation of the surface integral (last term) in Eq. (9) in the discretised form, which represents the frictional effect of solid skeleton on the macroscopic flow field.

Equation (11) is the general SPH form of the momentum equation for flow through porous media, while different closure models have been introduced and employed in the literature for the estimation of the friction term \mathbf{A}_a . In the present study, Ergun's equation (Ergun, 1952) is employed as shown in Eq. (12), where c_1 and c_2 are empirical constants, ν is the fluid kinematic viscosity, and d_s is the mean diameter of particles in the porous media. The turbulent shear stress term is estimated by using the SPS model (Gotoh et al., 2001) as

presented in Eq. (13), where $\nu_{t,a}$, \mathbf{S}_a , and $k_{t,a}$ are the turbulent eddy-viscosity, the strain tensor, and the SPS turbulent kinetic energy, respectively, at the position of particle a . The turbulent eddy viscosity is estimated as $(C_s\Delta)^2|\mathbf{S}_a|$, where C_s is the Smagorinsky constant and Δ is the filter width. Since the filtered velocity in the view of LES is the same as the average/macroscopic velocity in the present work (see Appendix A), setting the filter width to the particle spacing l_0 (which is a common practice in SPH simulations) seems to be reasonable. Moreover, the equation of state is employed to compute the pressure of a particle explicitly from the change in its density according to Eq. (14), where ρ_0 is the reference density and c_0 is the speed of sound which is chosen to restrict the compressibility of flow to be less than 1%. The determination of all these coefficients for the present simulations will be discussed in the model applications (Section 3.1).

$$\mathbf{A}_a = -c_1 \frac{(1 - \phi_a)^2}{\phi_a^2} \frac{\nu}{d_s^2} \mathbf{u}_a - c_2 \frac{(1 - \phi_a)}{\phi_a} \frac{1}{d_s} \mathbf{u}_a |\mathbf{u}_a| \quad (12)$$

$$\left(\frac{\boldsymbol{\tau}}{\rho}\right)_a = -2\nu_{t,a}\mathbf{S}_a + \frac{2}{3}k_{t,a}\mathbf{I} \quad (13)$$

$$P_a = c_0^2(\rho_a - \rho_{0,a}) \quad (14)$$

It is noted that the effect of particle volume change due to the change of porosity from one region to another has been taken into account in the derivation of Eqs. (10) and (11) by considering the volume of a particle to be equal to its mass divided by the product of its porosity and density. The porosity at particle a is approximated by the following equation which is the discretised form of $G * \gamma$.

$$\phi_a = (G * \gamma)_a \approx \sum_c G(\mathbf{r}_a - \mathbf{r}_c, h_\Omega) \gamma_c \Delta V_c \quad (15)$$

where the summation is computed over the background mesh; and γ_c denotes the value of the distribution function at mesh point c , which, according to Eq. (3), is either equal to one or zero dependent on whether the mesh point is located inside either the fluid or solid phases, respectively. ΔV_c is the volume of mesh element associated with the mesh point c that is equal to l_c^2 and l_c^3 in 2D and 3D domains, respectively, if one considers a regular mesh of points with spacing l_c . The mesh spacing should be chosen to be small enough to resolve the fluid-solid interfaces in porous media adequately.

2.4 Treatment of the interfacial boundaries

The model developed in the previous section can be applied to both 2D and 3D problems, and the system governed by Eqs. (10) and (11) constitutes a unified framework, i.e. the equations are solved in a single computational domain including the porous and free-flow regions. The change from one physical region to another is addressed by calculating the transition in the porosity. A fixed background mesh is therefore used that contains the information of the distribution function at each mesh point. To determine the porosity at the position of a particle volume, the distribution function is averaged over the background mesh using the weighting function G , given by Eq. (15). This function meets the *constraints #1, #2 and #3*.

However, *constraints #1 and #2* are not easily satisfied in the region near an interface with an external free-flow. One example is represented in Figure 1, which depicts a sheared interfacial layer between flow in a porous medium (region 1) and an overlying free-flow (region 3). Average flow quantity $\langle\psi\rangle^\alpha$ changes sharply over the relatively thin interface layer (region 2). This layer (the region between dashed-dotted lines in Figure 1) may correspond to the ‘roughness layer’ found in turbulent flow over rough boundaries, including the interfacial and form-induced sublayers, as defined by Nikora et al. (2001). In such a condition, the *constraints #1 and #2*, i.e. $L_\psi \ll r_\Omega \ll L_{\langle\psi\rangle^\alpha}$, are usually satisfied in region (1) since $L_{\langle\psi\rangle^\alpha}$ is much larger than L_ψ in this region by assuming that L_ψ is in the order of L_d (Figure 1, left), where L_d is a characteristic length scale of the solid matrix. However, the satisfaction of $L_\psi \ll r_\Omega \ll L_{\langle\psi\rangle^\alpha}$ in the interface layer (region 2) is not so straightforward because here L_ψ and $L_{\langle\psi\rangle^\alpha}$ may be in the same order ($\approx L_d$). Hence, in region (2), the best choice for the support of the weighting function G , would be $r_\Omega \approx L_{d,i}$, where $L_{d,i}$ is the characteristic length scale of solid matrix in the interfacial boundary. Besides, in region (3), there is no constraint in the computation of porosity as it is a constant (= 1.0) all over the free-flow region. Meanwhile, *constraint #3* and the constraints associated with the averaging process over the macroscopic field, i.e. *constraints #4 and #5*, are all valid.

In principle, the governing equations presented in Eqs. (10) and (11), with the porosity computation process presented through Eq. (15), along with the above constraints are the general form of SPH solutions for the interaction of free-flow with flow in porous media. However, in practical applications, due to unavoidable simplifications associated with the dimensional issue as well as the determination of porosity, a simpler form of the solution is usually adopted, e.g. in the previous SPH studies (such as Shao, 2010; Akbari and Namin, 2013; Gui et al., 2015; and Ren et al., 2016), the implications of which will be discussed in the following sections.

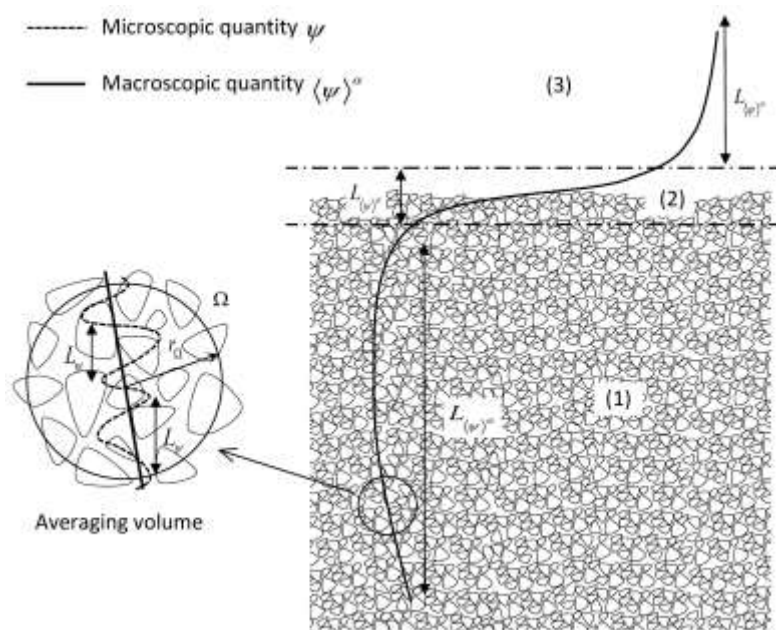


Figure 1. A schematic view of distribution of an arbitrary average flow quantity. (1), (2), and (3) denote the underlying porous media, the interface layer, and overlying free-flow regions, respectively.

In practical situations, the detailed microstructure of the porous media is often unknown and there is usually no definitive information about the fluid-solid interfaces so that the determination a priori of the distribution function for Eq. (3) is not always feasible. Moreover, applying Eq. (15) for computing the porosity needs a 3D representation of the distribution function γ . Hence, in practical numerical simulations, the porous media is usually assumed to be homogeneous and continuous; and accordingly, the definition of the distribution function (Eq. 3) is modified as follows,

$$\gamma = \begin{cases} 1.0 & \text{free-flow region} \\ \phi_0 & \text{porous media flow region} \end{cases} \quad (16)$$

where ϕ_0 is the mean value of porosity of the porous media which can be obtained in the laboratory as the volume of fluid a porous medium contains being divided by the total volume of the medium. In this case, the *constraints #1* and *#2* are instinctively satisfied in the porous region far from the interface boundary (region 1 in Figure 1) since the porosity is effectively constant in this region. This statement is also valid for the free-flow area far from the interface (region 3 in Figure 1), since the porosity is also constant ($\phi_0 = 1.0$) in this region.

Based on the above discussion, the constraints associated with the weighting function G (for averaging over the background mesh) as well as the constraints associated with the kernel function W (*constraints #4* and *#5* of r_γ) are all summarised below for the present practical situation.

- (a) $r_\Omega \approx L_{d,i}$ over the interface (This constraint for r_Ω is not required far from the interface where porosity is constant)
- (b) r_Ω and G should not change with time over the entire (Eulerian) domain
- (c) $r_\gamma \ll L_{\langle \mathbf{u} \rangle}^\alpha$, over the entire domain
- (d) r_γ and W should be set equally over space and should remain unchanged with time, over the entire (Lagrangian) domain

Note that point (c) (*constraint #4*) is written only in terms of the average velocity field, because this constraint is instinctively satisfied for all other flow quantities such as the density and pressure due to the incompressibility (or weakly compressibility) of flow. In other words, in the case of interaction of an incompressible (or weakly compressible) sheared flow with a porous medium, velocity is the only flow quantity which may have large variations over the interfacial boundary and therefore needs careful consideration with regard to the *constraint #4*. In SPH, the support of kernel function has a certain relation with the particle spacing (smoothing length is usually taken as 1.2 times the particle spacing), thus a sufficient computational resolution should satisfy the condition of $r_\gamma \ll L_{\langle \mathbf{u} \rangle}^\alpha$.

If adopting the present treatment, a boundary which separates the free-flow and porous regions should be defined so that Eq. (16) can be used for the determination of γ . This is not

an easy task particularly when the surface of the porous media is rough, namely, when the size of solid particles on the surface is of a similar scale compared with the characteristic dimensions of the free-flow layer (for example, the size of the internal flow structures). Figure 2a shows an arbitrary underlying porous medium with an overlying free-flow layer; and Figures 2b-d illustrates the determination of the interface boundary by separating the two regions using a line (namely, a ‘separating line’ in 2D or a ‘separating surface’ in 3D).

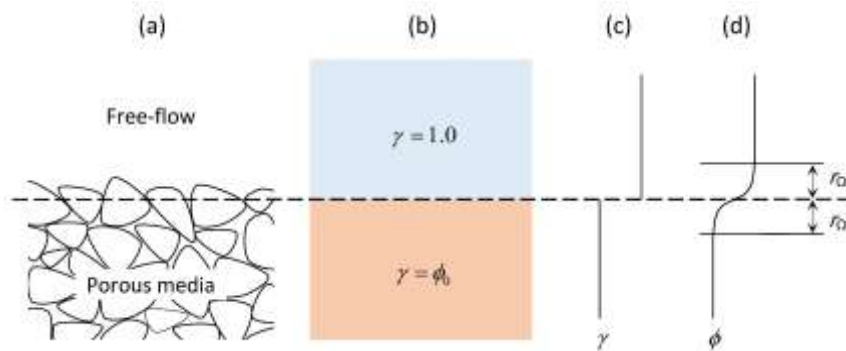


Figure 2. Determination of distribution function and porosity by the separating line in 2D condition. The dashed line represents an arbitrary separating line.

Determination of the location of the separating line depends strongly on the problem and the physical characteristics of the interface boundary as well as the prevalent flow conditions. One may consider the crest of solid particles at the interface as the separating line/surface. It seems a fair approximation when the surface is relatively smooth. However, one may consider the so called ‘zero-plane displacement’ level as the interfacial separating line, when the surface is rough. The concept of zero-plane displacement was discussed in detail by Nikora et al. (2002). Figure 2c shows the distribution of γ based on the separating line (which is schematically shown by a dashed line), while Figure 2d presents the distribution of porosity obtained by Eq. (15), which guarantees a smooth change of porosity at the interfacial boundary from the underlying porous media to the overlying free-flow region. The curvature of the porosity profile at the interface depends on the type of the weighting function G as well as its support size r_0 that is determined through Eq. (17). By using any symmetric weighting function, the inflection point of the porosity profile should always lie on the separating line.

2.5 Summary of the theoretical development

The above theoretical developments are briefly summarised as follows. Firstly, the microscopic governing equations (Eqs. 1 and 2) were spatially averaged using a weighting function G which satisfies certain conditions. The averaging process yielded the macroscopic governing equations presented in Eqs. (4) and (5) with specific geometrical constraints. The extra stress terms emerged in the equations represent the frictional effect of solid materials and the effect of turbulence on the macroscopic flow field. The ‘average velocity’ superimposes with the ‘LES filtered velocity’ since the turbulent shear stress term (which is modelled by the SPS model) has been developed through the spatially averaging process of the equations. Then, the macroscopic governing equations (Eqs. 4 and 5) were averaged again using a kernel function W , and then discretised based on the standard SPH formulations in Eqs. (10) and (11). During this process, $G * \gamma$ was considered as porosity ϕ and estimated by Eq. (15). To use this equation, one needs to have the values of the distribution function γ at nodal points of a background mesh. However, this is not always possible due to the difficulties in accurately measuring the characteristics of the microstructure of the porous media. Therefore, a pragmatic solution was introduced in Section 2.4, and the constraints reduced to those presented in Eq. (17). **Accordingly, the support of the weighting function G (for estimating the porosity on a background mesh) is not constrained in the constant-porosity free-flow and porous media regions far from the interface (i.e., the *constraints #1* and *#2* do not need to be satisfied in these two regions), but it needs to be of the order of the characteristic size of solid elements in the interface boundary region (Eq. 17a); and the support of the kernel function W used for the discretisation of the governing equations on the macroscopic field should be small enough to resolve all the variations in the average velocity field (Eq. 17c).** In other words, G , r_Ω and h_Ω should be set according to Eqs. (17a) and (17b) for the computation of porosity values on the background mesh (i.e. they should depend on the geometrical characteristics of the porous medium); and W , r_γ and $h_\gamma (= 1.2l_0)$ should satisfy the constraints in Eqs. (17c) and (17d) for the discretisation of the macroscopic domain and computation of the flow quantities at the position of SPH computational particles (i.e. they do not depend on the

geometrical characteristics of the porous medium, but should be selected to adequately capture the variations in the macroscopic field).

The aim of exploring the above theoretical basis of the problem was to provide a general form of the SPH governing equations for flow interaction with rough boundaries formed in porous media and clearly list the required constraints with those equations. Understanding the relevant assumptions and constraints with the solution procedure could help prevent the use of unjustified assumptions used when dealing with such physical situations as seen in previous studies. In the previous SPH porous flow applications, the choice of support size of the weighting function, determination of the thickness of the interfacial layer, and the separating line between the porous and free-flow regions have often been carried out instinctively rather than being based on rigorous mathematical justifications. For instance, Akbari and Namin (2013) interpolated the porosity with an r_Ω being about 4 times the solid particle diameter, which would be too large according to point (a) in Eq. (17); or in their numerical models, Ren et al. (2014) and Gui et al. (2015) set the thickness of the interfacial layer based on the numerical resolution (i.e., SPH kernel size) rather than the physical size of the solid particles forming the boundary surface of the porous media, which may not be accurate due to the same constraint. Another example is that, Pahar and Dhar (2017) used a non-constant smoothing length (i.e. averaging volume size in present context) since the inter-particle distance increases when the fluid particles move into areas with a lower porosity. This is actually in contradiction with the *constraint #5* (Eq. 17d). Also, in some of the previous studies discontinuities were introduced at the interfacial boundary and then an additional averaging process had to be performed to treat these discontinuities to enforce the continuity of the flow quantities.

Although some simplifications are unavoidable due to the dimensional and geometrical differences with the physical cases, the proposed model will be used for the solution of four engineering cases of flow interaction with the boundary of porous media.

3 Model Applications in Practical Porous Flow

The aim of this section is to test the numerical formulation developed previously, by simulating several benchmark applications demonstrating flow interaction with porous media. A 2D model based on the SPHAM equations (Eqs. 8 and 9) and discretised by Eqs. (10) and (11) is adopted. A two-step predictor-corrector solution scheme is applied in the time marching implementation. Four test cases are simulated, and the results compared with the published experimental data or analytical solutions to validate the accuracy of the model. The test cases include: i) Seepage flow in a U-tube filled with porous media; ii) dam break wave through a porous dam; iii) solitary wave interaction with a porous structure; and iv) solitary wave run-up on a smooth impermeable breakwater and a porous breakwater. These case studies have been selected to test the capacity of the model in dealing with the flow and wave interactions with structures of different porosities and surface characteristics. The first U-tube case is considered as a rigorous validation test of flow through a homogeneous porous media with available analytical solutions. The second dam break case is considered as a fundamental benchmark experimental test which has been employed in many previous numerical studies. In the experimental study of the third case, there is detailed velocity distribution data around and close to the boundary of a porous structure; and the fourth case study provides water surface elevation and velocity time series for the wave interaction of breakwaters, with similar shapes but different characteristics in terms of permeability.

3.1 Computational specifications

If the particle volume at a position with porosity ϕ_1 is ΔV_1 , its volume at a position with porosity ϕ_2 shall be $\phi_1 \Delta V_1 / \phi_2$. Therefore, if the initial particle spacing in the free-flow region (with porosity 1.0) is set to l_0 , then the initial spacing of a generic particle with porosity ϕ_a should be set according to the following relationship

$$l_a = \frac{l_0}{\sqrt[N]{\phi_a}} \quad (18)$$

where N is the number of dimensions (= 2 in the present model).

In all the present model applications, the situation presented in Section 2.4 is considered. By using Equation (16) for the determination of distribution function γ , Equation (15) will give constant values of 1.0 and ϕ_0 for porosity, respectively, in the free-flow and porous regions far from the interfacial boundary, independent of the size of support of the weighting function (r_Ω), since in those areas γ is constant within the averaging volume Ω . Therefore, the porosity at the position of particles in the pure fluid and pure porous regions is set to constant values of 1.0 and ϕ_0 ; and a background mesh with regular square elements is defined to cover only the required area at the interface where the porosity changes, instead of using this for the entire computational domain, to reduce the computational expense. The separating line is considered to be $0.5d_s$ away from the crest of the first line of solid particles at the interface towards the media. Following the length constraint in Eq. (17a), the diameter of the averaging volume Ω is set to d_s , i.e. $r_\Omega = 0.5d_s$ ($h_\Omega = 0.25d_s$). In fact, the thickness of the layer at the interface over which the porosity changes from ϕ_0 to 1.0 is equal to the mean diameter of the solid particles. The mesh spacing l_c is taken as $h_\Omega/1.2$ so that enough mesh points exist in the averaging volume Ω for the porosity calculation. Besides, the smoothing length of the kernel function W , i.e. $h_\gamma (= \frac{1}{2}r_\gamma)$, is set to $1.2l_0$ for all the simulations. As for the choice of l_0 , it is selected to satisfy the constraint in Eq. (17c). This issue will be further explored in Section 3.6. For both G and W , the cubic Spline kernel function of Monaghan and Lattanzio (1985) is used, which satisfies the required conditions presented in Sections 2.1 and 2.2.

For the impermeable wall boundaries, the ‘dynamic boundary condition’ (Dalrymple and Knio, 2001) is applied by placing three layers of dummy particles beyond the boundary line to fill the truncated kernel area in the vicinity of the boundary. The computational time step Δt is chosen according to the CFL stability condition. The dynamic and kinematic viscosity of fluid (ν and μ) are set to $10^{-6} \text{ m}^2.\text{s}^{-1}$ and $10^{-3} \text{ kg}.\text{m}^{-1}.\text{s}^{-1}$, respectively. The reference intrinsic density (ρ_0 in Eq. 14) is $1000 \text{ kg}/\text{m}^3$ and the speed of sound c_0 is set to $10\sqrt{9.81H_0}$ (where H_0 is the initial water depth) in order to restrict the compressibility to be less than 1%. c_0 is set equally in the entire computational domain. A Shepard density filter is applied at every 30 computational time steps to smooth the particle density, therefore minimise the pressure noises. The Smagorinsky constant C_s for the estimation of eddy-viscosity ν_t is set

to 0.1, and the filter width is set to the particle spacing l_0 . c_1 and c_2 in Eq. (12) are set to 150 and 1.75, respectively, as originally proposed by Ergun (1952). These values are used for all the application cases considering that they have been obtained from measurements of various flow conditions through the porous beds created using different particle sizes. The principle behind the choice of these constants is that it should be reasonable to tolerate the expected errors, if they are within an acceptable range, rather than constructing the model based on the arbitrary numerical tuning of calibration parameters within the equations used to describe specific physical processes.

3.2 Test case I: Seepage flow in a U-tube with porous media

The accuracy of the developed model is firstly verified by simulating a linear seepage flow in a U-tube containing a porous soil medium. The application set-up is the same as in Peng et al. (2017) and Khayyer et al. (2018). Water flows under the gravity due to a difference of water level in the left and right vertical sections of the U-tube, seeping through a porous soil medium placed in the centre of the horizontal section. Neglecting the non-linear frictional term (second term in Eq. 12), the analytical solutions for the water level difference (ΔH) and the Darcy velocity in the porous medium (U) are expressed as follows

$$\Delta H = \frac{\Delta H_0}{\exp(2K_h t/L)} \quad (19)$$

$$U = \frac{\Delta H_0 K_h}{\exp(2K_h t/L)L} \quad (20)$$

where t is the time; ΔH_0 is the initial water level difference (= 1.35 m); L is the seepage path length (= 1.0 m); and K_h denotes the hydraulic conductivity.

Numerical simulations are conducted with two different values for K_h (= 0.005 and 0.01 m/s). Initial particle spacing (l_0) in the free-flow (clear water) region is set to 3 mm, while inside the porous region, it is initially set according to Eq. (18). Porosity of the soil ϕ_0 is set to 0.4. The temporal changes in ΔH and U are computed and compared with the analytical solutions, as well as the SPH results of Peng et al. (2017) and Khayyer et al. (2018). The closure models employed in those studies for the frictional term in the momentum equation are different with the present model. Based on the definitions presented in those papers,

the friction term \mathbf{A}_a in the present study can be formulated as a function of the hydraulic conductivity as $\mathbf{A}_a = (g/K_h)\mathbf{u}_a$, where g is the gravitational acceleration ($= 9.81 \text{ m/s}^2$). Also note that the seepage velocity U in Eq (20) is equivalent to ϕu , where u is the component of the intrinsic average velocity.

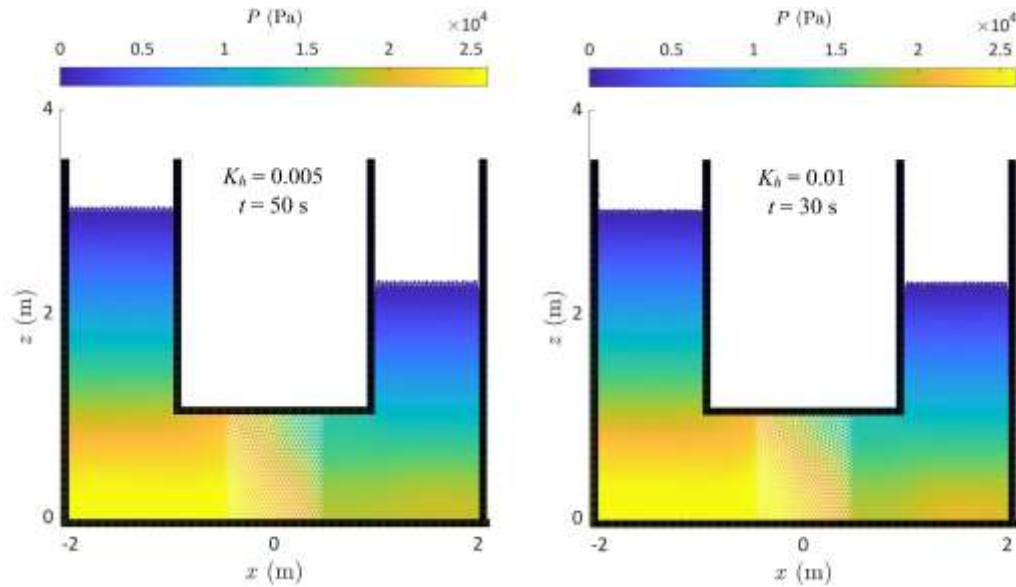


Fig. 3. Snapshots of particle position with pressure distribution for $K_h = 0.005 \text{ m/s}$ at $t = 50 \text{ s}$ (left), and $K_h = 0.01 \text{ m/s}$ at $t = 30 \text{ s}$ (right).

Figure 3 shows the simulation results of pressure distributions at $t = 50 \text{ s}$ for $K_h = 0.005 \text{ m/s}$, and $t = 30 \text{ s}$ for $K_h = 0.01 \text{ m/s}$. The present model provides smooth pressure distributions in the computational domain and especially near the interfacial boundaries. Figure 4 presents the time histories of variations of ΔH and U in comparison with the analytical solutions (Eqs. 19 and 20), as well as the WCSPH results by Peng et al. (2017) and ISPH results by Khayyer et al. (2018). Table 1 provides the Mean Absolute Error (MAE) values of these time histories relative to the analytical solutions. It shows that the best accuracy is associated with the results of Khayyer et al. (2018). Their model outperforms the other two, probably due to the incompressible and higher-order schemes used for solving the pressure. For example, by looking at Figure 3, one deficiency of the WCSPH computation is that the particle spacing increases in an unrealistic way near the water surface due to an inaccurate pressure estimation near the boundary. This is a common problem with the WCSPH solution scheme since the estimated pressure is not exactly zero at free surface boundaries. This could

inevitably cause errors in the estimation of ΔH and U . However, comparing the two WCSPH models, the results of the present model are more accurate than those of Peng et al. (2017), which could be attributed to the refined treatment of the interfacial porous boundary. Besides, the present results also clearly disclose the expansion of particles' volume inside the porous region, as shown in Figure 3.

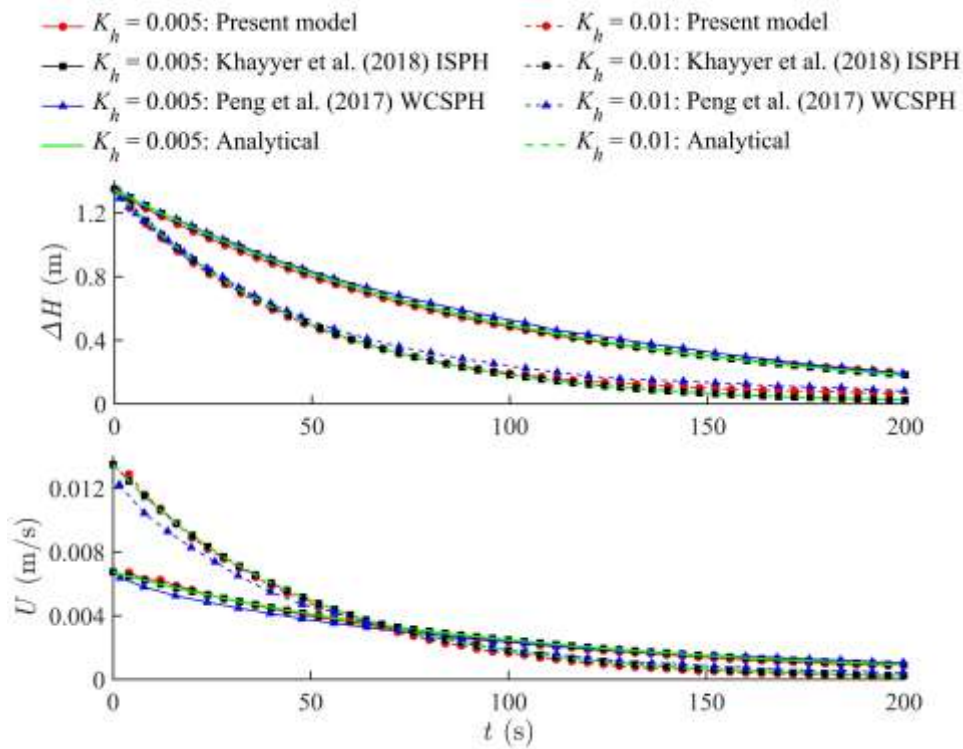


Figure 4. Time series of the variations of ΔH and U computed by the present model in comparison with the analytical solutions and SPH studies of Peng et al. (2017) and Khayyer et al. (2018).

Table 1. Mean Absolute Error (MAE) in time series of ΔH and U between the numerical and analytical solutions.

| | MAE of ΔH (m) | | MAE of U (m/s) | |
|------------------------------|-----------------------|--------------|------------------|--------------|
| | $K_h = 0.005$ | $K_h = 0.01$ | $K_h = 0.005$ | $K_h = 0.01$ |
| Present model – WCSPH | 1.36E-02 | 2.04E-02 | 1.15E-04 | 1.54E-04 |
| Khayyer et al. (2018) – ISPH | 6.90E-08 | 4.12E-08 | 3.23E-10 | 4.52E-10 |
| Peng et al. (2017) – WCSPH | 1.75E-02 | 3.52E-02 | 2.07E-04 | 3.11E-04 |

3.3 Test case II: dam break wave through a porous dam

The developed model is employed to simulate 2D dam break flow through a porous dam. The numerical results of free surface profiles are compared with the experimental data of Liu et al. (1999), where a small-scale porous dam constructed with crushed rocks was studied. The water tank was 89.2 cm long, 44 cm wide, and 58 cm high. The porous dam was 29 cm long, 44 cm wide, and 37 cm high. It was located at the centre of the tank, built by crushed rocks with a mean diameter of 1.59 cm (mean porosity $\phi_0 = 0.49$). A gate was placed 2 cm away from the upstream side of the dam. Initial water depth H_0 was 25 cm and the gate was opened manually within 0.1 s.

In the free-flow region the initial particle spacing (l_0) is set to 3 mm, while inside the porous dam, it is initially set according to Eq. (18). Fig. 5 presents snapshots of particle position and pressure distribution at different times. The computed pressure field is smooth both in the free-flow and porous regions as well as near the interfacial boundaries. Particle configurations near the upstream side of the dam, where the volume of particles changes while they move into the porous region, is shown at the bottom of Figure 5 for $t = 2.0$ s. Regularity of particle distribution near the interface boundary is clearly seen. Besides, the experimental water surface profiles are also shown in Figure 5 for a comparison. The Root Mean Square Error (RMSE), which represents a measure of the deviation of the numerical water surface profiles from the experimental data, is below 7 mm for all the times shown in Figure 5, except at $t = 0.2$ s and 0.4 s, where it is 15.7 and 8.5 mm, respectively. This may be due to the porous structure not being fully saturated so that the drag within the porous media was inaccurately estimated in the early stages of the experiment. In the later stages when the porous media was close to being fully saturated then Ergun's equations were more reliable.

In order to show the satisfaction of the volume conservation, the trajectories of three selected particles and the temporal changes of their density (ρ) and volume ($m/\phi\rho$) in the first 2.5 seconds of the simulation are depicted in Figure 6. These particles were initially located at horizontal positions of $x = 0.14, 0.20$ and 0.26 m, and vertical position of $z = 0.15$ m. During the first 0.5 seconds, it is shown that the fluid density fluctuates due to the collapse of water (and this fluctuation is higher for particle p_3 which is closer to the free

surface), then it stabilises and remains constant for all the three particles. Besides, Figure 6 also shows their volume changes when they move into or out of the porous region. The volume of particle p_1 remains constant as it never enters the porous area, while the volume of particle p_2 increases by a factor of about 2 at $t = 1$ s when it travels into the porous region. The volume of particle p_3 rises much earlier at $t = 0.1$ s when it enters the porous region but then drops to its initial value at about $t = 1.35$ s when it leaves the porous dam.

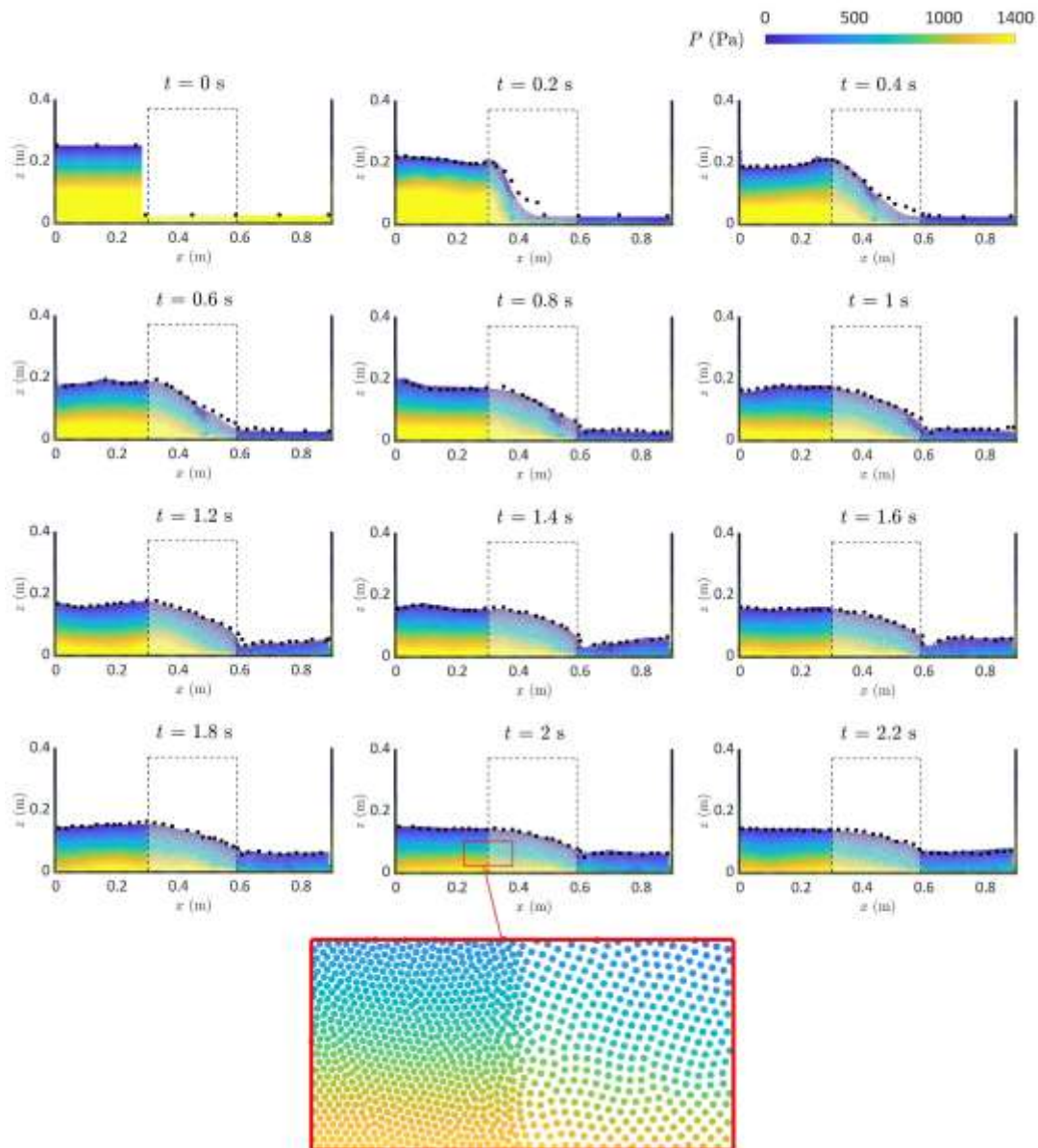


Fig. 5. Particle position and pressure distribution at different times for the dam break flow through crushed rocks. Black squares represent the experimental water surface profiles of Liu et al. (1999).

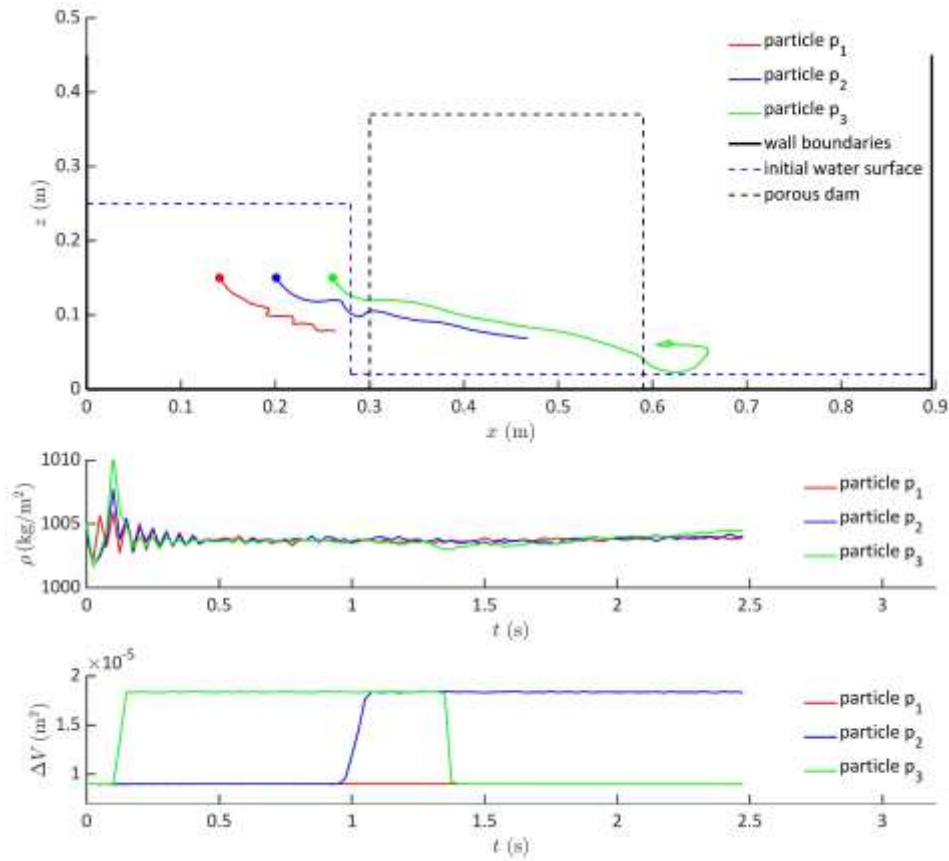


Fig. 6. Satisfaction of volume conservation: trajectories of three particles (top); temporal variations of their density (middle) and volume (bottom) during the first 2.5 seconds of simulation.

Figure 7 provides a further comparison between the present model results of water surface profile at time $t = 1.2$ s with some previous SPH studies and the experimental data of Liu et al. (1999). As can be seen, the present model and the model of Ren et al. (2016) provide better estimations compared with the studies of Akbari and Namin (2013) and Akbari (2014). This improvement is probably related to the treatment of the interfacial boundaries. In Akbari and Namin (2013) and Akbari (2014), the thickness of the interfacial transitional layer over which the porosity is variable was set to $4d_s$ (where d_s is the solid grain diameter), while in the present model as well as in Ren et al. (2016), the porosity changes over a layer with the thickness of d_s . This is due to that the averaging volume size Ω for the calculation of porosity in the present simulations was set based on constraint (a) in Eq. (17). Moreover, the comparisons of Ren et al. (2016) and present model results in Figure 7 reveal that in spite of using different values for the drag coefficients, the two computed water surface profiles are close to each other. This similarity can also be seen by comparing Akbari

and Namin (2013) and Akbari (2014) results. These comparisons suggest that a slight change in the drag coefficient does not considerably affect the results of water surface elevations, while the treatment of the interfacial boundaries could have a much greater influence.

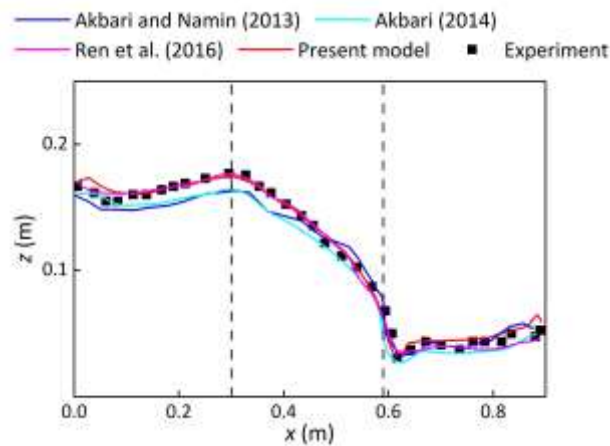


Figure 7. Comparisons of the present water surface profile with other SPH studies and experimental data of Liu et al. (1999). Dashed lines show the front and rear sides of the porous dam.

3.4 Test case III: solitary wave interaction with a porous structure

A set of data which provides detailed velocity profiles was used to further investigate the accuracy of the developed model. Wu and Hsiao (2013) studied the propagation of solitary waves over a submerged porous structure both experimentally and numerically. Their laboratory experiments were carried out in a 25 m long, 0.5 m wide and 0.6 m deep wave tank with the glass walls and bottoms. Figure 8a is a schematic view of the flume set-up. The wave tank was filled with water at a constant depth $H_0 = 10.6$ cm and solitary waves with three different heights were generated in the experiments. Here, only the result for the wave with height $H_w = 0.45H_0$ is presented. A submerged porous structure composed of spherical glass beads with diameter $d_s = 1.5$ cm and porosity $\phi_0 = 0.52$ was placed in the middle of the flume. The origin of the coordinate system ($x = 0, z = 0$) was considered at the intersection of the front side of the structure and the flume bottom as shown in Figure 8a, and the reference time $t = 0.0$ s was set when the crest of the wave arrives at the wave gauge 1 (WG₁ at $x = -1.8$ m). The horizontal and vertical velocity profiles were measured around the structure at different horizontal locations $x = -0.04, 0.0, 0.04, 0.08, 0.12, 0.16$

and 0.20 m and at different times $t = 1.45, 1.65, 1.85, 2.05$ and 2.25 s using a PIV system. Since the porous structure covers the whole width of the ‘narrow’ flume, this case can be simulated in 2D.

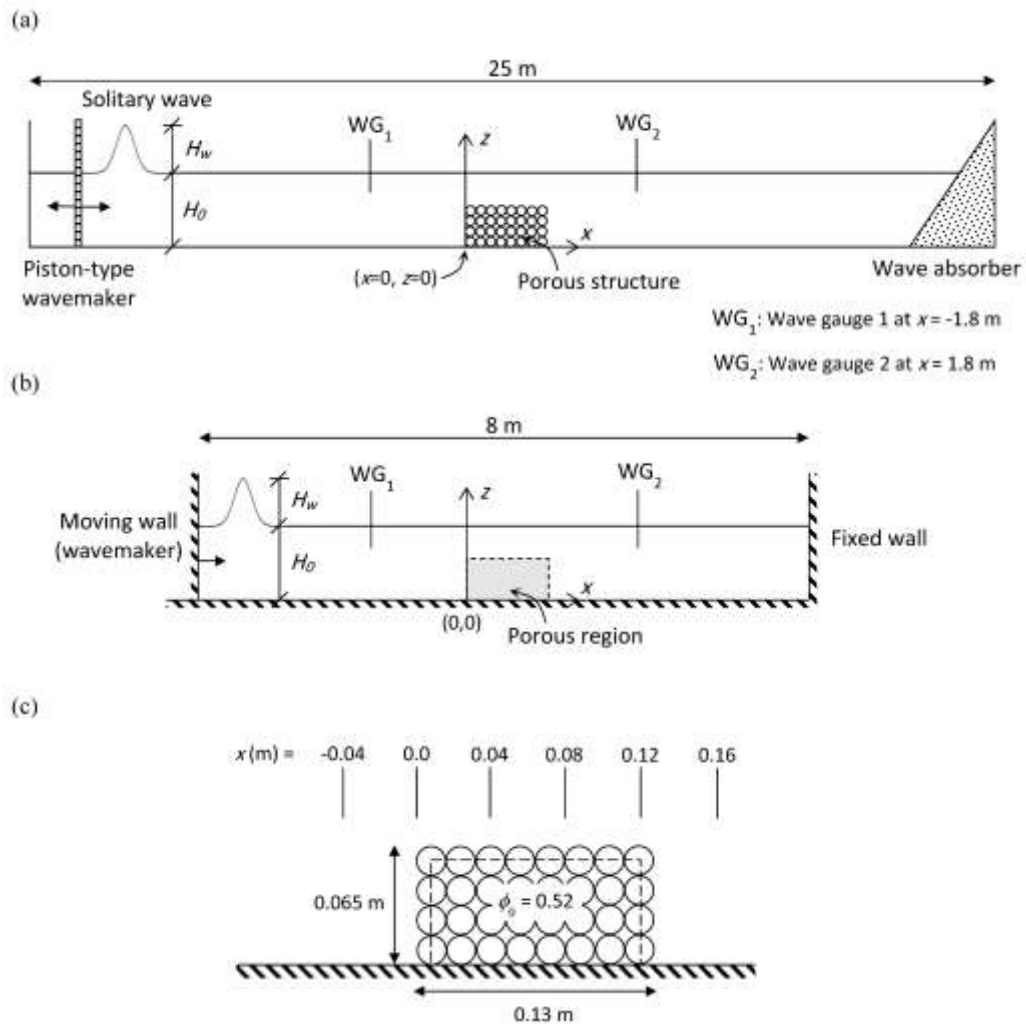


Figure 8. Experimental and numerical set-up for solitary wave interaction with a porous structure: (a) experimental flume of Wu and Hsiao (2013); (b) 2D computational domain of the present model; and (c) porous structure with the separating line and the locations of velocity profiles measurement.

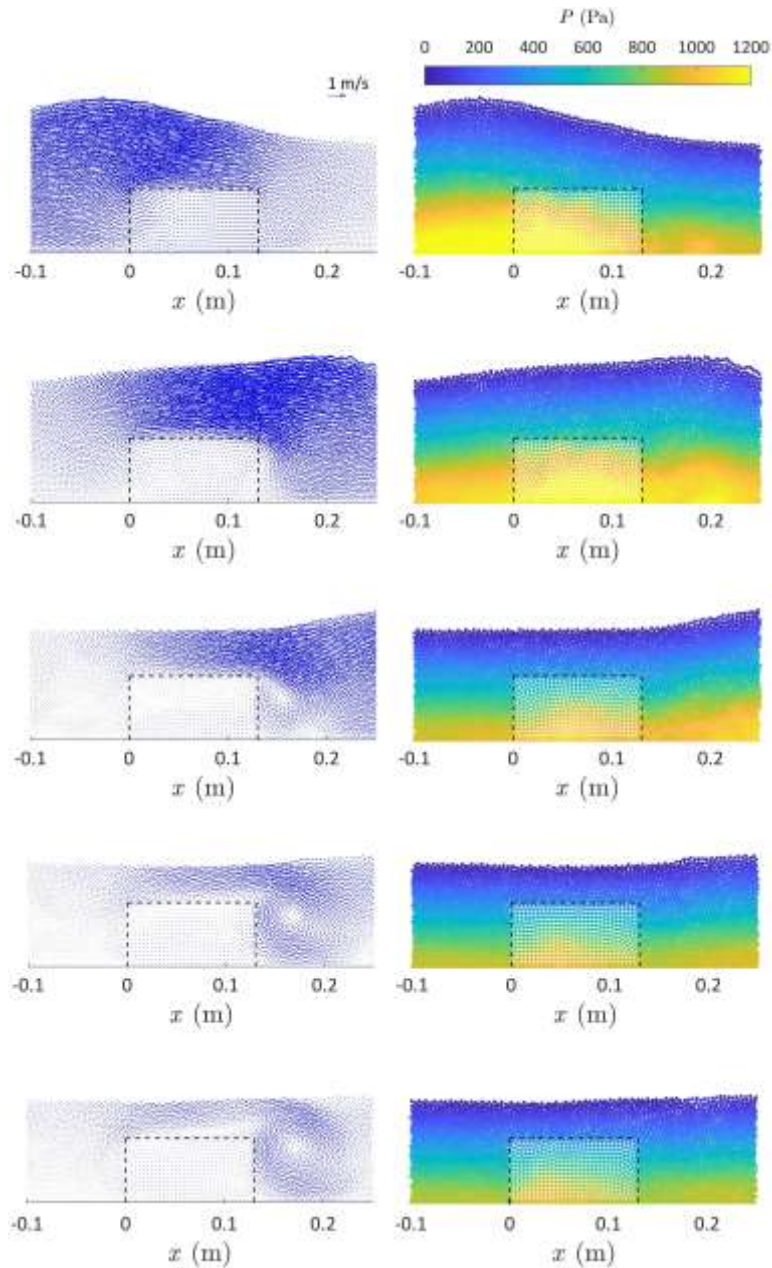


Fig. 9. Velocity vectors (left) and particle distributions with pressure field (right) around the porous structure at times $t = 1.45, 1.65, 1.85, 2.05$ and 2.25 s.

In the present model, a computational domain is chosen with the following characteristics. The initial particle spacing in the free-flow region (l_0) is set to 3 mm, while in the porous structure it is initially set according to Eq. (18). Following Gui et al. (2015) (who also simulated this test case using a 2D SPH model), a numerical wave tank is constructed with 8 m in length instead of simulating the 25 m long experimental wave tank (see Figure 8b) and a solitary wave with height 4.77 cm is generated at the wavemaker location ($x = -4.0$ m) to enable the numerical wave height to be matched with the measured one at the location of

the reference wave gauge WG_1 ($x = -1.8$ m). Figure 8c shows the porous structure, the locations where the velocity profiles are measured in the experiments, and the separating lines (dashed) as introduced in Section 2.4.

The numerical results of pressure field, velocity vector and turbulent shear stress distribution around the porous structure at different times $t = 1.45, 1.65, 1.85, 2.05$ and 2.25 s are presented in Figures 9 and 10, respectively. Although the accuracy of these computed distributions of pressure and turbulent shear stress cannot be validated directly due to the lack of experimental data, they are presented here to show the continuity of these quantities around and inside the porous structure. However, if one compares these pressure distributions qualitatively with the ones obtained by Khayyer et al. (2018), it is clear that the present results are not as smooth as the latter. This could be due to the superiorities of the projection-based ISPH method and the higher-order pressure solution scheme adopted in their work (Gotoh and Okayasu, 2017).

To validate the accuracy of the model in the reproduction of velocity field close to the porous structure, the velocity profiles at $x = 0.04, 0.08$ and 0.12 m (above the structure) at $t = 1.45, 1.65$ and 1.85 s (when the wave is travelling above the structure) are presented and compared with the experimental data of Wu and Hsiao (2013) (for comparisons at other times and sections refer to Kazemi, 2017). Figures 11 and 12 present the horizontal and vertical velocity profiles in comparison with the experimental profiles and Table 2 presents the MAE values of those profiles with respect to the experimental data. The MAE values were computed by fitting spline curves to both experimental and numerical profiles over the part of the depth where experimental data points are available. A reasonable agreement in terms of velocity magnitude and velocity gradient (in the vertical direction) is seen between the experimental data and predictions at all sections and times.

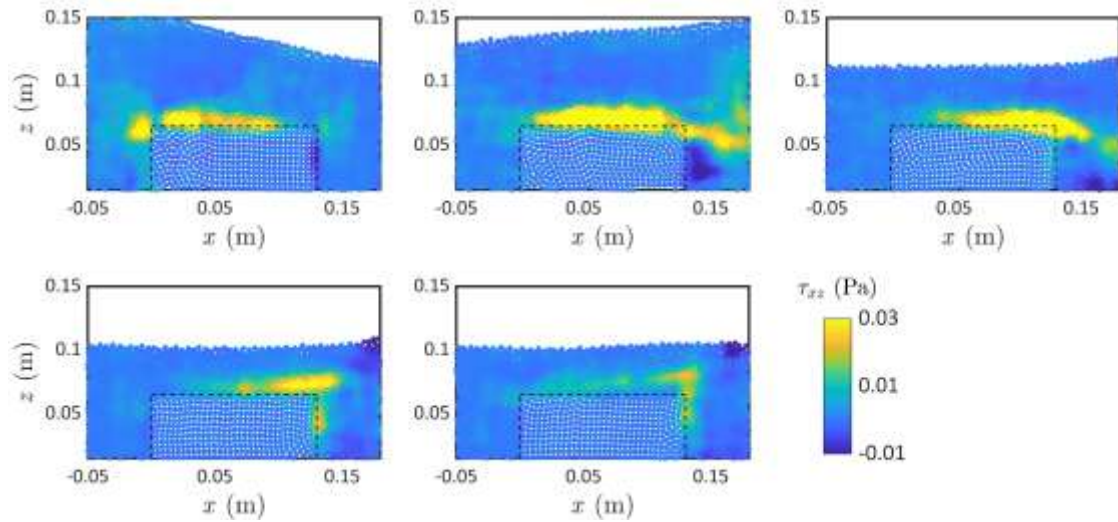


Fig. 10. Distributions of xz component of the predicted turbulent shear stress around the porous structure at times $t = 1.45, 1.65, 1.85, 2.05$ and 2.25 s.

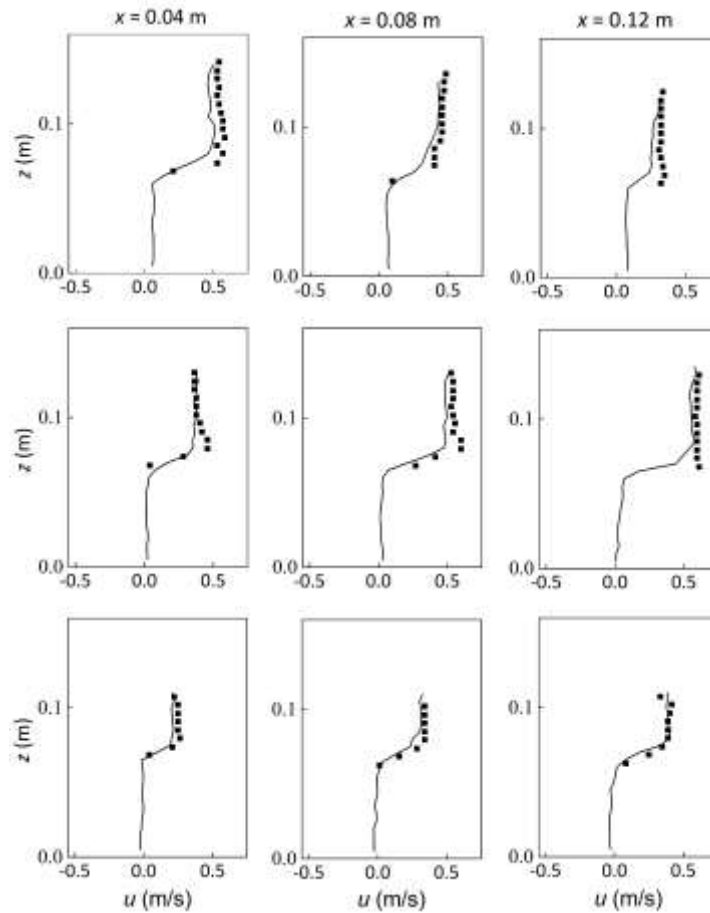


Figure 11. Numerical results of horizontal velocity profiles in comparison with the experimental profiles at $x = 0.04, 0.08$ and 0.12 m at times $t = 1.45$ (top), 1.65 (middle) and 1.85 s (bottom) – lines and squares denote numerical and experimental profiles, respectively.

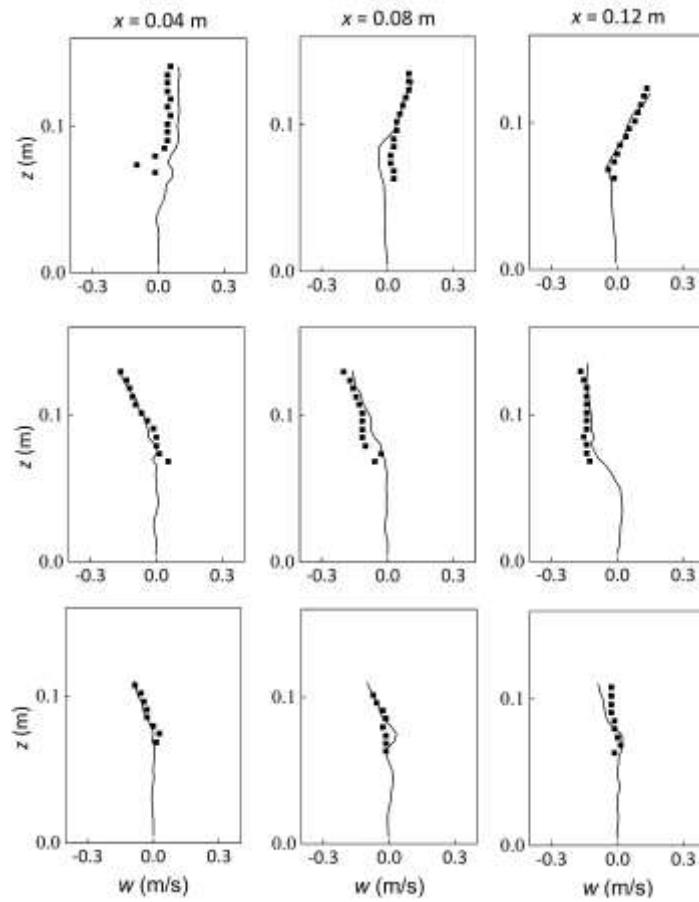


Figure 12. Numerical results of vertical velocity profiles in comparison with the experimental profiles at $x = 0.04, 0.08$ and 0.12 m at times $t = 1.45$ (top), 1.65 (middle) and 1.85 s (bottom) – lines and squares denote numerical and experimental profiles, respectively.

Table 2. MAE (m/s) of the computed horizontal and vertical velocity profiles, with respect to the experimental data.

| Time (s) | $x = 0.04$ m | | $x = 0.08$ m | | $x = 0.12$ m | |
|------------|------------------|------------------|------------------|------------------|------------------|------------------|
| | MAE _u | MAE _w | MAE _u | MAE _w | MAE _u | MAE _w |
| $t = 1.45$ | 0.079 | 0.060 | 0.049 | 0.029 | 0.063 | 0.014 |
| $t = 1.65$ | 0.039 | 0.015 | 0.071 | 0.035 | 0.057 | 0.022 |
| $t = 1.85$ | 0.037 | 0.016 | 0.048 | 0.022 | 0.033 | 0.028 |

In the ISPH simulations of the same case, Gui et al. (2015) used completely different relationships for the permeability and Forchheimer tensors in their drag closure model. Figure 13 compares the streamwise velocity profiles computed by the present SPH model in

comparison with the original ISPH results of Gui et al. (2015) and the experiments of Wu and Hsiao (2013) at different times and sections. The upper subplots show the profiles associated with time $t = 1.45$ s, when the wave is travelling above sections $x = 0.0$ and 0.04 m, and the lower subplots present the results associated with time $t = 1.65$ s when the wave is above sections $x = 0.08$ and 0.12 m. The figure shows that the present model provides better estimations of the velocity distribution above the structure while the wave is travelling over it. Inside the porous structure, both models provide similar velocity profiles, although different drag closure models have been used. However, at the interface boundary between the porous structure and free-flow region above it, the slope of the velocity profiles is found to be closer to the experimental data when simulated by the present model than Gui et al. (2015), and this effect also leads to a better prediction of velocity distribution above the structure.

This is further quantified in Table 3, where the MAE values of streamwise velocity (u) and its gradient ($\partial u/\partial z$) are presented for both Gui et al. (2015) and the present study, with respect to the experimental data. The MAEs of velocity are calculated over the entire depth (subject to the availability of the experimental data), and the velocity gradient MAEs are those only at the interface layer where the velocity has a significant change. This comparison shows that a small improvement in the predicted velocity gradient at the interface boundary can cause significant improvements in the computed velocity field in the overlaying flow. Gui et al. (2015) used a transitional layer at the interface with a thickness of 4 times of the SPH particle spacing and averaged the SPH pressures over this layer to smooth out the flow quantities at the interface. On the other hand, in the present model, the thickness of the interface layer over which the porosity changes from ϕ_0 to 1.0, is chosen based on the characteristic length scale of the solid skeleton at the interface (to satisfy the constraint in Eq. 17a) rather than being related to the computational resolution. It is also notable that Gui et al. (2015) ignored the effect of particle volume change in the continuity equation.

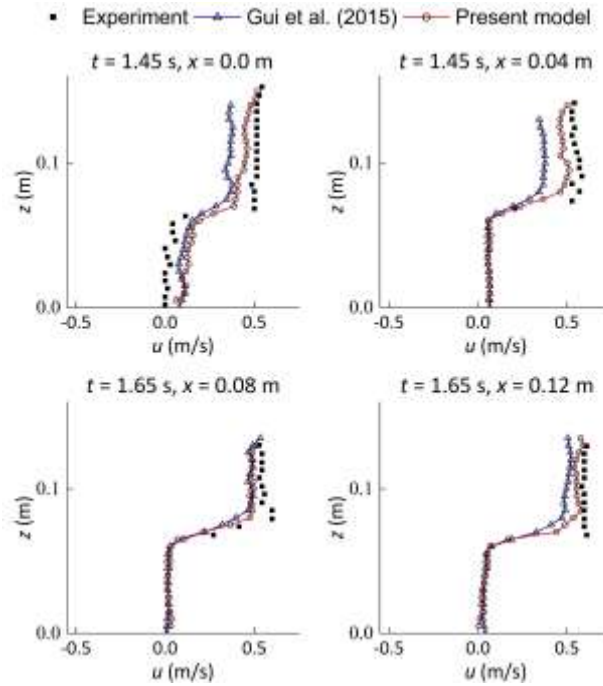


Figure 13. Streamwise velocity profiles computed by the present model in comparison with the ISPH results of Gui et al. (2015) and experiments of Wu and Hsiao (2013) at different sections and times.

Table 3. MAE of the velocity (m/s) its gradient (1/s) for both Gui et al. (2015) and present studies, with respect to the experimental data. (MAE of velocity gradient at $t = 1.65$ s and $x = 0.12$ m is not calculable due to the lack of experimental data within the interface layer or below it)

| | MAE _u (m/s) | | MAE _{∂u/∂z} (1/s) | |
|----------------------------|------------------------|---------------|----------------------------|---------------|
| | Gui et al. (2015) | Present study | Gui et al. (2015) | Present study |
| $t = 1.45$ s, $x = 0.0$ m | 0.126 | 0.083 | 39.73 | 34.66 |
| $t = 1.45$ s, $x = 0.04$ m | 0.183 | 0.079 | 40.61 | 37.08 |
| $t = 1.65$ s, $x = 0.08$ m | 0.086 | 0.071 | 15.35 | 10.24 |
| $t = 1.65$ s, $x = 0.12$ m | 0.119 | 0.057 | n/a | n/a |

3.5 Test case IV: solitary wave run-up on smooth impermeable and porous breakwaters

In this section, the model is applied to the case in which a solitary wave runs up and down on a breakwater slope based on the experiments of Jensen et al. (2015). The experiments were carried out in a 25 m long, 0.6 m wide and 0.8 m deep flume. The still water depth (H_0) was fixed to 0.4 m and a solitary wave with height of $H_w = 0.14$ m was generated in all

experiments. Figure 14a shows a schematic view of the experimental set-up. In Jensen et al. (2015), wave run-up and run-down on breakwaters with smooth impermeable and rough surfaces, and a porous breakwater was tested. For the case of a smooth impermeable surface, the breakwater slope was made out of a plastic PVC plate with a width of 0.6 m corresponding to the flume width. For the case of the rough breakwater surface, the plate was covered by an armour layer of single plastic spherical particles with diameter $d_s = 38$ mm. For the case of porous breakwater, the same type and size of the spheres were used to construct the breakwater core and the plastic PVC plate was replaced by a 2 mm thick perforated plate. Values of 0.40 and 0.41 were reported for the porosity of the core materials and the void-to-plate ratio (porosity) of the perforated plate, respectively. To measure the water surface elevation pattern, two wave gauges were set up, one being at the upstream side of the breakwater and another at the toe of the breakwater (WG_o and WG_t , respectively, in Figure 14a), in which the latter was considered as the reference gauge. The velocity was measured at two sections above the breakwater surface at several points. The measurement sections and their distances to the toe are shown in Figure 14b. The results of water surface elevations at WG_t and slope-parallel velocity profiles at measurement section I (at 2 and 19 mm above the slope surface for the smooth case, and at 2 and 57 mm above it for the rough and porous cases) are reported in Jensen et al. (2015).

The proposed 2D SPH model is employed to simulate a solitary wave run-up and run-down on the slope of the smooth impermeable and porous breakwaters (Figure 14c). The case of the breakwater with the rough surface is not considered here due to the ‘unrealistic’ conditions in the physical experiment in which the porosity changed from 0 to 1 within a short distance from the breakwater surface (i.e., within a layer of single plastic spherical particles with diameter $d_s = 38$ mm). This case could not be simulated well by the present numerical model as it is designed to macroscopically simulate flow in smooth and continuous interface layers with a relatively coarse computational resolution.

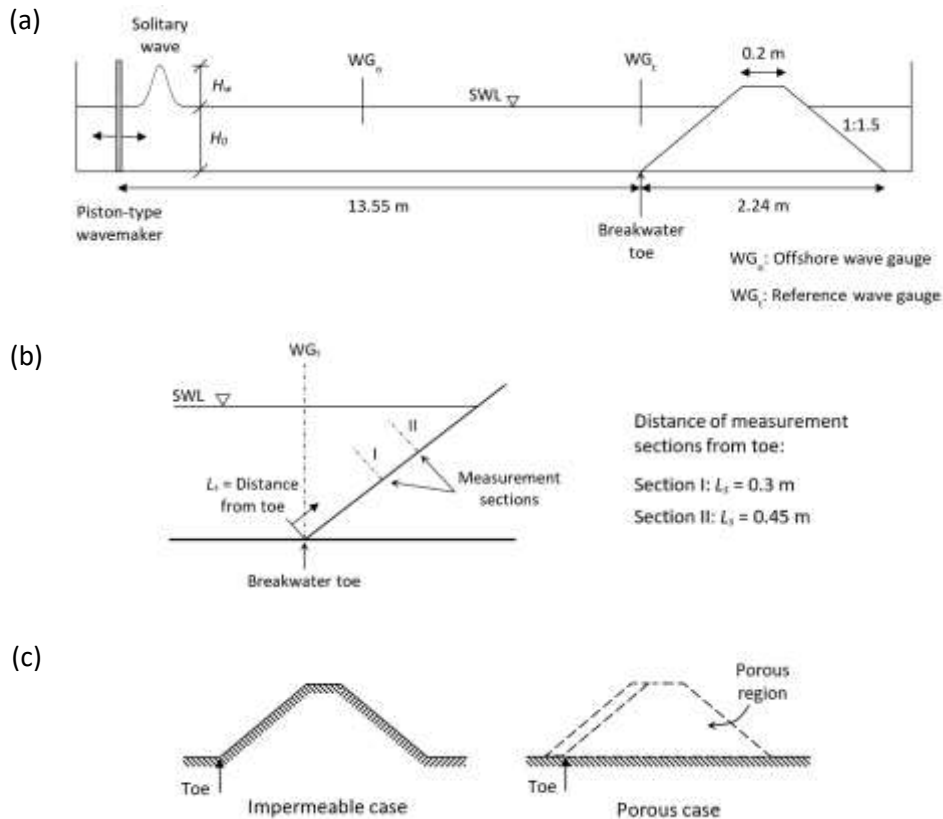


Figure 14. Experimental and numerical set-ups for solitary wave run-up on impermeable and porous breakwaters: (a) experimental flume of Jensen et al. (2015); (b) measurement sections; and (c) numerical configuration of breakwater boundaries for smooth impermeable and porous cases (hatched areas show the solid wall boundaries).

For the present simulations, the initial particle spacing in the free-flow region l_0 is 10 mm. Three layers of fixed dummy particles are placed adjacent to the wall boundaries as depicted by the hatched areas in Figure 14c. For the case of the smooth impermeable slope, as there is no porous region in the domain, the porosity of all fluid particles is set to the unity and no background mesh is needed. For the porous case, both the armour layer and the breakwater core are considered as porous regions with a uniform porosity of 0.4.

Figure 15 presents the computed water surface elevations at the breakwater toe, and the slope-parallel velocities at section I (19 mm above the slope for the impermeable case and 57 mm above it for the porous case) in comparison with the experiments of Jensen et al. (2015). $t = 0$ is defined when the wave crest arrives at the reference gauge (i.e., breakwater

toe). The RMSE values of the computed water surface elevations η with respect to the experimental data at the toe of the breakwater (between -2 and 4 s) for the smooth impermeable and porous breakwaters are 0.0142 and 0.0145 m, respectively; and the RMSEs of the computed slope-parallel velocities u for those cases (between $t = -2$ and 4 s) are 0.063 and 0.089 m/s, respectively.

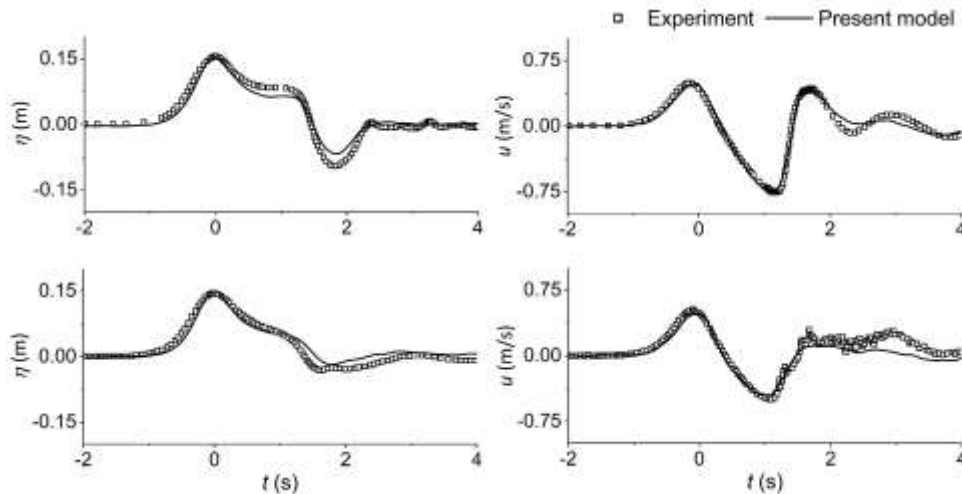


Figure 15. Water surface elevation (η) at the toe, and slope-parallel velocity (u) on the smooth impermeable (top) and porous (bottom) breakwaters at Section I (19 mm and 57 mm above the slope for the impermeable and porous cases, respectively) between $t = -2.0$ and 4.0 s.

To further investigate the effect of porosity on the wave run-up and run-down, the computed water surface elevations and velocity profiles for both cases, i.e. impermeable and porous breakwaters, are presented together in Figure 16. According to this figure, the water surface elevation in the porous case is only a few millimetres less than the impermeable case when the wave is running up, while the difference becomes significantly higher during the run-down and secondary run-up. Besides, the variation of the parallel-slope velocities is much larger on the impermeable slope but smaller when the breakwater is porous as the secondary run-up can be barely observed. This is attributed to the penetration of water into the porous structure so that a significant part of the momentum in the slope-parallel direction is removed due to the permeability of the breakwater slope.

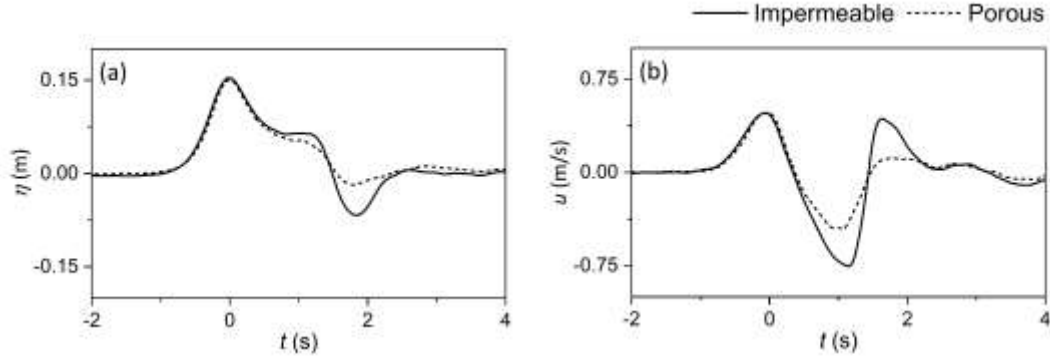


Figure 16. Comparison of numerical results of (a) water surface elevation at the breakwater toe; and (b) slope-parallel velocity at 19 mm and 57 mm above the slope for the smooth impermeable and porous cases, respectively.

3.6 Sensitivity analysis of computational resolution at the interface layer

It has been discussed that if the situation introduced in Section 2.4 is adopted, the required constraints are those represented in Eq. (17). However, the satisfaction of *constraint #4* (or Eq. 17c, i.e. $r_\gamma \ll L_{(u)\alpha}$) may not always hold in certain simulations. According to this constraint, the kernel support size r_γ should be much smaller than the characteristic length scale of the averaged flow field. Since in SPH, r_γ is related to the particle spacing ($h_\gamma = 1.2l_0$ as a common practice), l_0 should be chosen as to satisfy *constraint #4*. To further investigate this issue, the previous test cases II and III are revisited here with different particle spacing.

Figure 17 presents the comparison of water surface profiles of the test case II (dam break wave through the crushed rocks) at time $t = 1.2$ s by using different particle spacing. No considerable differences are seen among these profiles. This is due to the following possible factors: i) the flow Re Number is relatively low; and ii) the interfacial boundary between the porous and free-flow regions is not ‘sharp’ or highly sheared, i.e. no significant changes take place in the average flow quantities transferring from the free-flow region to the porous structure, and vice versa. Therefore, *constraint #4* should have been well satisfied with the adopted computational particle resolutions.

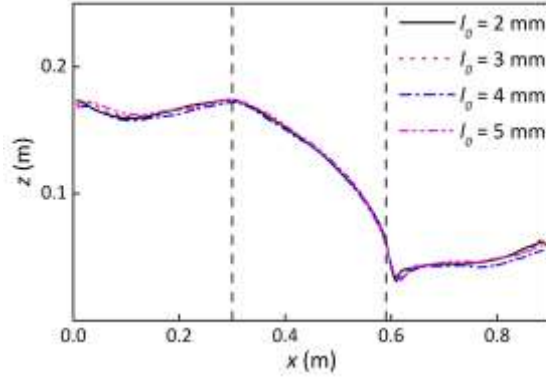


Figure 17 Water surface profiles of test case II (dam break wave through crushed-rock porous dam) using different computational resolutions (i.e., particle spacing l_0). The two vertical dashed lines show the boundaries of the porous dam.

However, the situation of the test case III is quite different. By looking at the experimental data of Wu and Hsiao (2013), and assuming that the velocity in the porous region is much smaller than that above the structure, the horizontal velocity shows a significant change over a thin layer at the interface. This can be seen more clearly at times $t = 1.45$ s and 1.65 s, when the wave is travelling rapidly above the porous structure. For instance, at $t = 1.45$ s and $x = 0.0$ m (refer to Kazemi, 2017), the measured horizontal velocity increases from about 0.04 m/s to 0.5 m/s over about 10 mm vertical layer distance at the interface. Another example can be seen at $t = 1.65$ s and $x = 0.12$ m (refer to Figure 11), where the experimental horizontal velocity has a relatively larger value of 0.61 m/s only about 2.5 mm above the structure boundary (spheres' crest). To resolve such a thin boundary in order to satisfy the *constraint #4*, a range of small kernel support size is required, particularly for the velocity, i.e. $r_\gamma \ll L_{\langle u \rangle}^\alpha$.

To investigate this issue in a quantitative manner, the simulation of test case III is repeated by using different initial particle spacing l_0 of 3 , 4 , 5 and 6 mm. Figure 18 shows the results in comparison with the experimental data at selected times and locations. In this figure, the horizontal and vertical velocity profiles at sections $x = 0.0$ and 0.04 m at $t = 1.45$ s, when the wave is travelling above the frontal edge of the structure, and at sections $x = 0.08$ and 0.12 m at $t = 1.65$ s, when the wave is passing the end of the structure, are presented. Some differences can be observed in the slope of the profiles at the interface. This can be seen more clearly from Figure 19, where the horizontal velocity profiles at $t = 1.65$ s and $x = 0.12$

m and vertical velocity profiles at $t = 1.45$ s and $x = 0.0$ m are plotted at a different scale. As the particle spacing is set to a smaller value (i.e., the spatial resolution gets higher), it shows the slope of velocity profiles becomes closer to the experimental one. The relationship between the initial particle spacing (l_0) and the Mean Relative Error, Err (Wang et al., 2019), of the horizontal velocity profiles at $t = 1.45$ s, $x = 0.04$ m and $t = 1.65$ s, $x = 0.12$ m, with respect to the experimental data, is shown in Figure 20. The error is calculated in the interface layer (between $z = 0.05$ and 0.1 m). The dashed lines show linear fit to the bold curves, and the numbers on the curves show the slope of the lines of linear fit. The slope, which represents the convergence rate, is 1.24 and 1.34, respectively, at these two sections. This figure quantitatively denotes that by reducing the particle spacing, the error also declines, and this process is nearly linear. This is due to the fact that by using a smaller particle spacing the satisfaction of *constraint #4* (Eq. 17c) at the interface can be approximately approached. Although this constraint may not be fully satisfied in such cases with ‘sharp’ interfacial boundaries, the errors should not be significant, which means the model is capable of reproducing satisfactory results in interface layers as shown in the present applications.

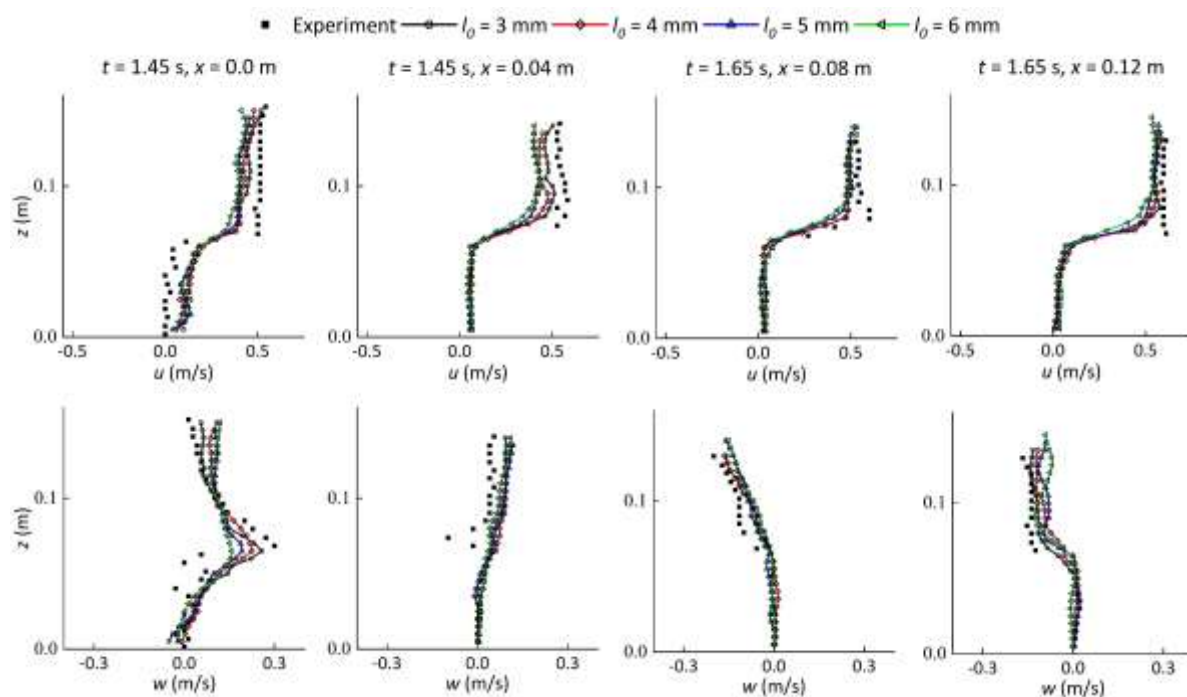


Figure 18. Horizontal (top) and vertical (bottom) velocity profiles with different particle spacing l_0 in comparison with the experimental data.

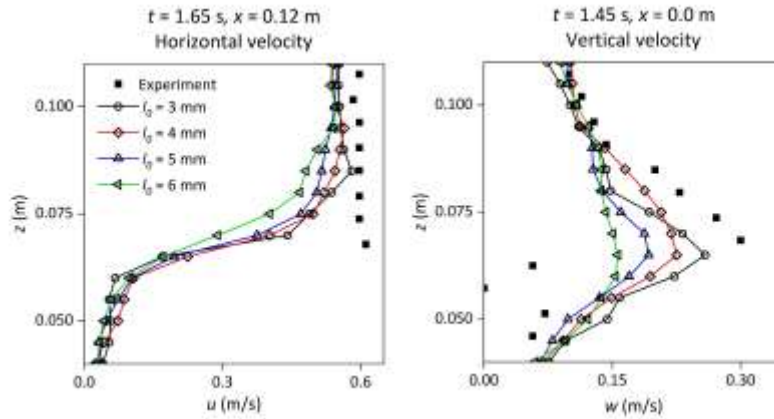


Figure 19. Horizontal velocity profiles at $t = 1.65$ s and $x = 0.12$ m (left) and vertical velocity profiles at $t = 1.45$ s and $x = 0.0$ m (right) with different particle spacing l_0 in comparison with the experimental data.

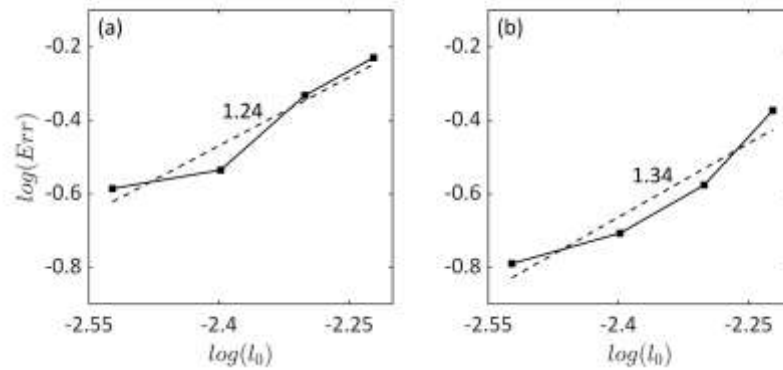


Figure 20. Error analysis and convergence rate for horizontal velocity at: (a) $t = 1.45$ s, $x = 0.04$ m; and (b) $t = 1.65$ s, $x = 0.12$ m.

4 Summary and Conclusions

Firstly, the macroscopic equations of flow through porous media, and over regions of variable porosity were developed with a rigorous insight into the assumptions and constraints required to ensure the valid application of the equations. Two distinct averaging operators (G and W) were used in order to distinguish between the determination of porosity at the microscopic scale and the calculation of flow quantities at the macroscopic scale. The equations are basically developed in 3D. However, in Section 2.4, a practical situation of 2D flow interaction within and above porous media was introduced and the determination of porosity as well as the modification of the length constraints were

investigated. The most important constraints were found to be that i) the support of the weighting function applied to the porosity calculation should be selected based on the characteristic length scale of solid boundary elements at the interface; ii) the computational resolution should be fine enough near the interface boundaries to adequately capture the variations in the macroscopic velocity field; and iii) the size of the averaging volume (smoothing length) applied to the solution of the governing equations should be set equally over the space and should remain unchanged over the time.

Then, after the desirable macroscopic equations, the closure models, and the relevant numerical treatments were available, and the limitations and constraints of all these were clear, a 2D WCSPH model was developed and four test cases of flow interaction with porous structures were simulated. The treatment of the interfacial boundary was carried out carefully in order to address the proposed mathematical requirements. The first case was a benchmark test with available analytical solutions; the second case was another benchmark which has been used in numerous studies to validate numerical models in predicting water surface elevations; the third one was selected to test the accuracy of the model in predicting velocity fields, particularly near the porous interface boundaries; and the fourth one was employed to examine the simulation of wave run-up over two different types of the porous and non-porous slopes. In the sensitivity analyses, the effect of computational resolution was investigated to check the validity of the equations at the interfacial boundaries with regard to the length constraints introduced in the theoretical justification.

It was shown that, i) satisfactory results are obtained in the different applications using Ergun's equations with its original coefficients; ii) the accuracy of model predictions depends heavily on the accuracy of the interface boundary treatment; for example, in the simulation of dam break flow through porous dams (test case II), it was observed that the interfacial boundary treatment is more important than a slight change in the drag coefficients when the porous material is fully saturated; and iii) the satisfaction of the required length constraint $r_\gamma \ll L_{(u)}^\alpha$ becomes more demanding when the flow Reynolds Number is higher and/or the velocity gradient is larger at the interfacial boundary. In the model sensitivity analysis, it was found that employing a higher resolution of the particles does not have a considerable effect on the results of water surface elevations in case of the

dam break flow through porous dams (test case II), while it significantly affects the results of velocity distributions near a porous structure while a wave is travelling over it (test case III).

It should be notable that although the SPS turbulence model (Gotoh et al., 2001) was applied with the Smagorinsky approach to estimate the eddy-viscosity, due to the unavailability of detailed turbulence data it was not possible to investigate the accuracy of the proposed turbulence closure scheme in the present applications, particularly its effect at the interfacial boundaries. The investigation of this issue requires more detailed data on the pattern of fluid turbulence at such interface boundaries. Moreover, as indicated in Sections 3.2 and 3.4, one of the limitations of the present model might be associated with the WCSPH scheme for the estimation of pressure. By utilising some more advanced numerical treatments, such as the ISPH higher-order pressure solution scheme (Gotoh et al., 2014; Gotoh and Khayyer, 2016) or the Optimised Particle Shifting technique (e.g. Khayyer et al., 2017), the performance of the present model would be expected to improve.

5 Acknowledgement

This work was supported by the Research Executive Agency, through the 7th Framework Programme of the European Union, Support for Training and Career Development of Researchers (Marie Curie — FP7-PEOPLE-2012-ITN), which funded the Initial Training Network (ITN) HYTECH ‘Hydrodynamic Transport in Ecologically Critical Heterogeneous Interfaces’, No. 316546.

Appendix A. Spatial averaging process for deriving the macroscopic governing equations

An averaging volume Ω which may contain both the fluid and solid materials (denoted by α and β , respectively) is considered. It is assumed that the solid phase is fixed in time and space. The SPH local volumetric average of a quantity ψ over the averaging volume Ω is given in Eq. (A.1). The averaging is associated with the centroid of the volume, \mathbf{r} , while the integration over Ω is performed by using a weighting function $G(\mathbf{r} - \mathbf{r}', h_\Omega)$, in terms of the

relative position vector $\mathbf{r} - \mathbf{r}'$ and a smoothing length h_Ω , where \mathbf{r}' denotes the position vector of the points other than the centroid.

$$\langle \psi \rangle^\Omega = \int_{\Omega} G(\mathbf{r} - \mathbf{r}', h_\Omega) \gamma(\mathbf{r}') \psi(\mathbf{r}') d\mathbf{r}' = G * (\gamma\psi) \quad (\text{A.1})$$

This equation represents the macroscopic description of ψ over Ω . $\langle \cdot \rangle^\Omega$ is the volumetric averaging operator and $G * (\gamma\psi)$ denotes the convolution product of $\gamma\psi$ using the weighting function G . It is common to use a cellular average operator for the local volumetric averaging in the derivation of the macroscopic equations. However, the aim of the present work was to derive those equations based on the weighted average form presented in Eq. (A.1), which is consistent with the SPH formulations.

In order to derive the macroscopic equations, the microscopic equations (Eqs. 1 and 2) need to be averaged by using Eq. (A.1). Therefore, the convolution product of G and each term in the equations is constructed. Then, there is a need to relate the average of the derivative of a quantity to the average of that quantity itself. Quintard and Whitaker (1993, 1994) developed a weighted function version of the spatial averaging theorem for such a purpose. Their theorem was derived based on the concept of ‘cellular average’. Using the SPH averaging principles, the following similar form of the theorem is obtained for the spatial and temporal derivatives, respectively.

$$G * (\gamma \nabla \psi) = \nabla [G * (\gamma \psi)] + G * (\psi \mathbf{n}_{\alpha\beta} \delta_{\alpha\beta}) \quad (\text{A.2})$$

$$G * \left(\gamma \frac{\partial \psi}{\partial t} \right) = \frac{\partial}{\partial t} [G * (\gamma \psi)] - G * (\psi \mathbf{u}_{\alpha\beta} \cdot \mathbf{n}_{\alpha\beta} \delta_{\alpha\beta}) \quad (\text{A.3})$$

These two equations are used to formulate the convolution product of G and each of the terms in Eqs. (1) and (2). The final form will be obtained as in Eqs. (4) and (5) as the macroscopic governing equations. The derivation process is lengthy and tedious, thus, interested readers are invited to read Kazemi (2017) for full details of the derivations. In the derivation process, the linear terms were obtained in a similar way as in Quintard and Whitaker (1994) where the Stokes equations were averaged. Accordingly, the surface integral term (last term on the right-hand side of Eq. 5) emerged through the averaging process of the pressure gradient and viscous terms (first and third terms on the right-hand

side of Eq. 2). The turbulent shear stress term (the fifth term on the right-hand side of Eq. 5) was obtained through the averaging process of the non-linear term in Eq. (2). The process of this term which led to the SPS modelling of turbulence is described briefly in the following.

Representing the velocity product in the non-linear convective term (second term on the left-hand side of Eq. 2) as $\mathbf{u}\mathbf{u} = \mathbf{u}\mathbf{u} - \langle \mathbf{u} \rangle^\alpha \langle \mathbf{u} \rangle^\alpha + \langle \mathbf{u} \rangle^\alpha \langle \mathbf{u} \rangle^\alpha$, constructing the convolution product of G and the non-linear convective term, and applying Eq. (A.2) and the no-slip condition (*assumption #2*) yields

$$\nabla \cdot [G * (\gamma \rho \mathbf{u}\mathbf{u})] = \nabla \cdot [G * (\gamma \rho \langle \mathbf{u} \rangle^\alpha \langle \mathbf{u} \rangle^\alpha)] + \nabla \cdot [G * (\gamma \boldsymbol{\tau})] \quad (\text{A.4})$$

where $\boldsymbol{\tau} = \rho \mathbf{u}\mathbf{u} - \rho \langle \mathbf{u} \rangle^\alpha \langle \mathbf{u} \rangle^\alpha$. The term $G * (\gamma \boldsymbol{\tau})$ represents the effect of deviations on the average/filtered field. It is noted that the intrinsic averages of velocity in the convolution product inside the first derivative term on the right-hand side of the above equation are evaluated at positions other than the centre of the averaging volume. Therefore, writing the Taylor series expansion for one of the intrinsic velocity components and considering *assumption #3* and *constraint #2* (which are written under Eqs. 4 and 5), it can be shown that

$$\begin{aligned} \nabla \cdot [G * (\gamma \rho \mathbf{u}\mathbf{u})] &= (G * \gamma) \langle \rho \rangle^\alpha \langle \mathbf{u} \rangle^\alpha \cdot \nabla \langle \mathbf{u} \rangle^\alpha + (G * \gamma) \langle \mathbf{u} \rangle^\alpha \langle \mathbf{u} \rangle^\alpha \nabla \langle \rho \rangle^\alpha \\ &+ \langle \rho \rangle^\alpha \langle \mathbf{u} \rangle^\alpha \cdot \nabla [(G * \gamma) \langle \mathbf{u} \rangle^\alpha] + \nabla \cdot [(G * \gamma) \langle \boldsymbol{\tau} \rangle^\alpha] \end{aligned} \quad (\text{A.5})$$

where $\langle \boldsymbol{\tau} \rangle^\alpha = \langle \rho \rangle^\alpha \langle \mathbf{u}\mathbf{u} \rangle^\alpha - \langle \rho \rangle^\alpha \langle \langle \mathbf{u} \rangle^\alpha \langle \mathbf{u} \rangle^\alpha \rangle^\alpha$ is the SPS stress tensor representing the effect of turbulence on the macroscopic flow field. Some of the terms in the above equation will be omitted while converting the local time derivative to the material derivative, and finally the term $-\nabla \cdot [(G * \gamma) \langle \boldsymbol{\tau} \rangle^\alpha]$ appears on the right-hand side of the averaged equation (Eq. 5). This extra stress term should be modelled by an appropriate closure model, such as the eddy viscosity based SPS, since it still contains the product of point values of the velocity. Since the development of the above turbulent stress term has been made through the averaging process of the macroscopic equations, the present concept of ‘averaged/macroscopic velocity’ superimposes with that of the ‘LES filtered velocity’. In the study of Hu et al. (2012), also, the spatial averaging theory was used (but based on a non-weighted cellular averaging concept) for porous flow simulation. They used identical box-filter to volume-average and simulate large eddies; and similar to the present study, in the

formulation of the turbulence effect, their concept of averaged velocity and filtered velocity superimposed with each other.

References

Akbari, H., 2014. Modified moving particle method for modeling wave interaction with multi layered porous structures. *Coastal Engineering* 89, 1-19.

Akbari, H., Namin, M.M., 2013. Moving particle method for modeling wave interaction with porous structures. *Coastal Engineering* 74, 59-73.

Dalrymple, R., Knio, O., 2001. Sph modelling of water waves, in: *Proceedings of the Coastal Dynamics*, Lund, Sweden. pp. 11-15.

Ergun, S., 1952. Fluid flow through packed columns. *Chemical Engineering Progress* 48, 89-94.

Gotoh, H., Khayyer, A., 2016. Current achievements and future perspectives for projection-based particle methods with applications in ocean engineering. *Journal of Ocean Engineering and Marine Energy* 2, 251-278.

Gotoh, H., Khayyer, A., 2018. On the state-of-the-art of particle methods for coastal and ocean engineering, *Coastal Engineering Journal* 60, 79-103.

Gotoh, H., Khayyer, A., Ikari, H., Arikawa, T., Shimosako, K., 2014. On enhancement of Incompressible SPH method for simulation of violent sloshing flows. *Applied Ocean Research* 46, 104-115.

Gotoh, H., Okayasu, A., 2017. Computational wave dynamics for innovative design of coastal structures. *Proceedings of the Japan Academy. Series B, Physical and Biological Sciences.* 93, 525–546.

Gotoh, H., Shibahara, T., Sakai, T., 2001. Sub-particle-scale turbulence model for the MPS method - Lagrangian flow model for hydraulic engineering. *Advanced Methods for Computational Fluid Dynamics* 9, 339-347.

Gray, W.G., 1975. A derivation of the equations for multi-phase transport. *Chemical Engineering Science* 30, 229-233.

Gui, Q., Dong, P., Shao, S., Chen, Y., 2015. Incompressible SPH simulation of wave interaction with porous structure. *Ocean Engineering* 110, Part A, 126-139.

Hu, K.C., Hsiao, S.C., Hwung, H.H., Wu, T.R., (2012) Three-dimensional numerical modeling of the interaction of dam-break waves and porous media. *Advances in Water Resources* 47, 14-30.

- Huang, C.J., Chang, H.H., Hwung, H.H., 2003. Structural permeability effects on the interaction of a solitary wave and a submerged breakwater. *Coastal Engineering* 49, 1-24.
- Jensen, B., Christensen, E.D., Sumer, B.M., Vistisen, M., 2015. Flow and turbulence at rubble mound breakwater armor layers under solitary wave. *Journal of Waterway, Port, Coastal, and Ocean Engineering* 141, 04015006.
- Kazemi, E., 2017. Numerical Modelling of Turbulent Free Surface Flows Over Rough and Porous Beds Using the Smoothed Particle Hydrodynamics Method. PhD thesis, University of Sheffield. <http://etheses.whiterose.ac.uk/id/eprint/19579>
- Khayyer, A., Gotoh, H., Shimizu, Y., 2017. Comparative study on accuracy and conservation properties of two particle regularization schemes and proposal of an optimized particle shifting scheme in ISPH context. *Journal of Computational Physics* 332, 236-256.
- Khayyer, A., Gotoh, H., Shimizu, Y., Gotoh, K., Falahaty, H., Shao, S., 2018. Development of a projection-based SPH method for numerical wave flume with porous media of variable porosity. *Coastal Engineering* 140, 1–22.
- Liu, P.L.-F., Lin, P., Chang, K.A., Sakakiyama, T., 1999. Numerical modeling of wave interaction with porous structures. *Journal of Waterway, Port, Coastal, and Ocean Engineering* 125, 322–330.
- Monaghan, J.J., Lattanzio, J.C., 1985. A refined particle method for astrophysical problems. *Astronomy & Astrophysics* 149, 135-143.
- Nikora, V., Goring, D., McEwan, I., Griffiths, G., 2001. Spatially averaged open-channel flow over rough bed. *Journal of Hydraulic Engineering* 127, 123-133.
- Nikora, V., Koll, K., McLean, S., Dittrich, A., Aberle, J., 2002. Zero-plane displacement for rough-bed open-channels flows. *International Conference on Fluvial Hydraulics, River flow, Louvain-la-Neuve, Belgium*, pp. 83-92.
- Pahar, G., Dhar, A., 2016. Modeling free-surface flow in porous media with modified incompressible SPH. *Engineering Analysis with Boundary Elements* 68, 75-85.
- Pahar, G., Dhar, A., 2017. On modification of pressure gradient operator in integrated ISPH for multifluid and porous media flow with free-surface. *Engineering Analysis with Boundary Elements* 80, 38–48.
- Peng, C., Xu, G., Wu, W., Yu, H., Wang, C., 2017. Multiphase SPH modeling of free surface flow in porous media with variable porosity. *Computers and Geotechnics* 81, 239–248.
- Quintard, M., Whitaker, S., 1993. Transport processes in ordered and disordered porous media: volume-averaged equations, closure problems, and comparison with experiment. *Chemical Engineering Science* 48, 2537-2564.
- Quintard, M., Whitaker, S., 1994. Transport in ordered and disordered porous media II: Generalized volume averaging. *Transport in Porous Media* 14, 179-206.

Ren, B., Wen, H., Dong, P., Wang, Y., 2014. Numerical simulation of wave interaction with porous structures using an improved smoothed particle hydrodynamic method. *Coastal Engineering* 88, 88-100.

Ren, B., Wen, H., Dong, P., Wang, Y., 2016. Improved SPH simulation of wave motions and turbulent flows through porous media. *Coastal Engineering* 107, 14-27.

Shao, S., 2010. Incompressible SPH flow model for wave interactions with porous media. *Coastal Engineering* 57, 304-316.

Wang, L., Khayyer, A., Gotoh, H., Jiang, Q., Zhang, C., 2019. Enhancement of pressure calculation in projection-based particle methods by incorporation of background mesh scheme, *Applied Ocean Research* 86, 320-339.

Wang, L., Wang, L.P., Guo, Z., Mi, J., 2015. Volume-averaged macroscopic equation for fluid flow in moving porous media. *International Journal of Heat and Mass Transfer* 82, 357–368.

Whitaker, S., 1969. Advances in theory of fluid motion in porous media. *Industrial and Engineering Chemistry* 61, 14-28.

Wu, Y.T., Hsiao, S.C., 2013. Propagation of solitary waves over a submerged permeable breakwater. *Coastal Engineering* 81, 1-18.